

**Flocculation effect on turbidity flows generated by deep-sea mining  
A numerical study**

Elerian, Mohamed; Huang, Ziyang; van Rhee, Cees; Helmons, Rudy

**DOI**

[10.1016/j.oceaneng.2023.114250](https://doi.org/10.1016/j.oceaneng.2023.114250)

**Publication date**

2023

**Document Version**

Final published version

**Published in**

Ocean Engineering

**Citation (APA)**

Elerian, M., Huang, Z., van Rhee, C., & Helmons, R. (2023). Flocculation effect on turbidity flows generated by deep-sea mining: A numerical study. *Ocean Engineering*, 277, Article 114250. <https://doi.org/10.1016/j.oceaneng.2023.114250>

**Important note**

To cite this publication, please use the final published version (if applicable).  
Please check the document version above.

**Copyright**

Other than for strictly personal use, it is not permitted to download, forward or distribute the text or part of it, without the consent of the author(s) and/or copyright holder(s), unless the work is under an open content license such as Creative Commons.

**Takedown policy**

Please contact us and provide details if you believe this document breaches copyrights.  
We will remove access to the work immediately and investigate your claim.



# Flocculation effect on turbidity flows generated by deep-sea mining: A numerical study

Mohamed Elerian<sup>a,\*</sup>, Ziyang Huang<sup>a</sup>, Cees van Rhee<sup>a</sup>, Rudy Helmons<sup>a,b</sup>

<sup>a</sup> Section of Offshore and Dredging Engineering, Faculty of Mechanical, Maritime and Materials Engineering, Delft University of Technology, Delft, the Netherlands

<sup>b</sup> Section of Mineral Production and HSE, Department of Geoscience and Petroleum, Faculty of Engineering, Norwegian University of Science and Technology (NTNU), Trondheim, Norway

## ARTICLE INFO

### Keywords:

Deep sea mining  
Polymetallic nodules  
Flocculation modelling  
Flocculation effect  
Population balance equation

## ABSTRACT

We have developed and investigated a hydrodynamic model of Deep-Sea Mining (DSM) collector turbidity flows that captures sediment particle aggregation and breakup. Flocculation is expected to have a significant impact on determining the spread patterns of the turbidity flows and the resulting turbidity currents. The recently validated drift-flux model by Elerian et al. (2022) has been coupled to the Population Balance Equation (PBE) for modelling real-life discharge scenarios. This advanced approach accounts for the dynamics of flocculation and offers a comprehensive simulation of discharge systems. We hypothesize that this will produce a more accurate representation of DSM turbidity flows in the near-field region, where the turbulence mixing is expected to be the highest. Particular emphasis is placed on the settling velocity closure, as the flocs that form are porous and have a complex geometry. The flocculation parameters are calibrated using the experiments of Gillard et al. (2019). Finally, we investigate the effect of flocculation in the near-field region by numerically solving the new model in a computational domain of the near-field region. The results indicate that aggregation is the primary mechanism, however, it does not have a visible impact on the turbidity flow in the immediate vicinity, but it is likely to have a substantial effect on the far-field region.

## 1. Introduction

In recent years, Deep-Sea Mining (DSM) has garnered significant attention globally due to the growing difficulties in metal supply chains. As a result, companies are seeking innovative ways to secure raw minerals. Deep-sea deposits contain highly sought-after minerals a, including Cobalt (Co), Nickel (Ni), Tellurium (Te), Titanium (Ti), Platinum (Pt) and rare Earth metals, that are in high demand among green technology manufacturers, resulting in a significant increase in interest in DSM in recent decades. There are various types of deposits in the deep sea, but some of the most important mineral resources are the potato-sized rocks known as polymetallic nodules. A typical mining system for such nodules consists of three components: a Polymetallic Nodule Mining Tool (PNMT), a Production Support Vessel (PSV), and a Vertical Transport System (VTS). The PNMT collects the nodules and separates them from the accompanying water–sediment mixture. The nodules are then transported to the PSV via the VTS, while the excess water–sediment mixture is discharged through the PNMT, resulting in a sediment plume (Alhaddad et al., 2022). These plumes and the corresponding increase in turbidity levels are one of the main environmental concerns associated with Deep-Sea Mining (DSM) (Sharma, 2015).

Due to the difficulties in conducting in-situ testing, our understanding of the generated turbidity flows is limited. Direct measurements of these flows are rare because of turbulence in the wake region, the complexity of measuring the impingement zone, and the limited research on the interaction between discharged plumes and plumes from tracks. The focus of this study is to examine the flocculation in the discharged mixture, which is still a subject of ongoing research with numerous uncertainties and areas for further exploration. Lab experiments are crucial in this regard, as they allow for calibration and validation of numerical models to predict the behaviour of turbidity flows in near and far regions (Elerian et al., 2021). Modelling of local characteristics of generated turbidity currents, such as velocity and concentration, is crucial for environmental impact predictions in DSM studies. Such predictions should be based on credible data. In this context, we aim to partially fill the current knowledge gap about the behaviour of particles in the near-field region by creating a new modelling approach that predicts turbidity flow dispersion in that area.

Early studies investigating DSM turbidity flows have been reported in the literature (Zielke et al., 1995; Jankowski et al., 1994; Purkiani et al., 2021), but, to date, there have been few near-field numerical

\* Corresponding author.

E-mail address: [m.f.a.i.elerian@tudelft.nl](mailto:m.f.a.i.elerian@tudelft.nl) (M. Elerian).

investigations dealing with DSM-generated turbidity flows. Decrop and Wachter (2019) presents a comprehensive two-phase CFD simulation of a PNMT discharge scenario, taking into account a variety of realistic conditions. Recently, Ouillon et al. (2021) conducted DNS simulations for a moving PNMT discharge process using the Boussinesq approach. This approach solves for a transport equation for buoyancy, along with Navier–Stokes and continuity equations. The results showed that when the PNMT's forward velocity is higher than the current's velocity, the forward velocity of the resulting turbidity current agrees with what is observed in lock-exchange tanks. While these studies give a basic understanding of the turbidity current structure in the near-field region, they do not consider the multiple particle size fractions and their interactions, such as aggregation and break-up processes. This could result in an incorrect estimation of particle settling velocity, which plays a significant role in determining the plume's behaviour.

When particles collide in the presence of organic material and are in a cohesive state, they can form a structure known as a “floc” through a process called “flocculation”. Recently, researchers have recognized that flocculation plays a crucial role in DSM turbidity flows (Gillard et al., 2019; Spearman et al., 2020; Muñoz-Royo et al., 2022; Helmons et al., 2022; Gillard and Thomsen, 2019; Ali et al., 2022). Interestingly, Gillard et al. (2019) showed in a controlled laboratory experiment that under specific mixing conditions, the median particle size ( $d_{50}$ ) of a CCZ (Clarion Clipperton Fracture Zone) sediment mixture can increase from 12  $\mu\text{m}$  to 600  $\mu\text{m}$  within just 7 min, indicating a rapid aggregation process between sediment particles. This leads to the firm conviction that flocculation could potentially serve as a crucial solution in reducing the impact of turbidity flows.

Shear-induced flocculation of multi-fraction sediment is primarily influenced by aggregation and break-up mechanisms, as revealed through experiments and numerical modelling of particle size distribution (PSD). Considerable effort has gone into developing a mathematical description of flocculation mechanisms, resulting in the creation of the “Population Balance Equation (PBE)” (Hounslow et al., 1988). PBE has gained widespread adoption among researchers in multiple fields for analysing flocculation processes under fixed flow shear rates (Quezada et al., 2020; Ruan et al., 2021; Jeldres et al., 2015; Maggi, 2009; Mietta et al., 2011). The results obtained from PBE have been shown to have a strong correlation with experimental findings (Cahill et al., 1987; Russel et al., 1991; Fernández-Barbero et al., 1996). As most engineering problems are dynamic, with changing flow conditions over time, researchers often couple Computational Fluid Dynamics (CFD) models with PBE to efficiently analyse mixture dynamics and particle-size changes simultaneously (Bhole et al., 2008; Silva et al., 2008; Golzarjalal et al., 2018; Shi et al., 2019). These studies employ an Euler–Euler modelling approach, treating the water–sediment mixture as separate fluid and solid fractions based on size, as interpenetrating continua. PBE is coupled with the Euler–Euler model and both are solved simultaneously, resulting in a computationally intensive process. Each particle fraction requires its own momentum equation and PBE, adding to the complexity of solving the source terms that couple the momentum equations for both the liquid phase and the particle fraction.

In contrast to other models that treat particle fractions as separate phases, the drift-flux model takes a mixture approach, where the entire mixture is represented by a single momentum equation. However, this approach requires the inclusion of a phase transport equation for each particle fraction (Goeree, 2018). Furthermore, the drift-flux model has been applied in different engineering applications (Van Rhee, 2002; Alhaddad et al., 2020; Decrop and Wachter, 2019; Goeree, 2018; Elerian et al., 2022; de Wit et al., 2014), supporting our choice for the model. To the best of our knowledge, the drift-flux model has been coupled with PBE in previous studies by Shen et al. (2018) and Chen et al. (2006), but both used only two or three phase PBE, which may affect the accuracy of predictions on a high-resolution grid. As shown in the work of Elerian et al. (2022), increasing the number of fractions leads

to improved accuracy in predicting the forward velocity of turbidity currents. However, the suitability of their approach depends on the type of problem being studied and the desired outcomes. Our investigation focuses on the near-field region, with a higher resolution in the spatial, temporal, and phase domains than has been studied in previous works. This higher resolution has implications for the details of turbulence modelling and, in turn, flocculation modelling.

Building on the findings of Gillard et al. (2019), we have developed a new numerical model to improve the accuracy of turbidity-flow prediction behind a PNMT. This model includes the calibration of the most critical flocculation parameters. Our model's predictive capability stems from the combination of the drift-flux modelling approach, validated by Elerian et al. (2022), implemented in OpenFOAM, and the population balance modelling approach developed by Hounslow et al. (1988). The coupling of these two approaches would enhance the model's accuracy in predicting turbidity-flow. This will yield an improved understanding of turbidity flows in the near-field, from which we can gain insights into how discharge parameters impact the mixture dispersion in the near and far field regions. This could open up new opportunities for engineering solutions to address this issue. The paper begins by calibrating the most important flocculation parameters of the PBE using the experimental work of Gillard et al. (2019) in Section 2. The effects of flocculation are then demonstrated in a real-world case study in Section 3. Conclusions are drawn in Section 4.

## 2. Numerical model

The mathematical description of the flow of water–sediment mixtures, such as DSM turbidity flows, is given by the variable-density, in-compressible Navier–Stokes equations. In the context of multi-phase flow, it is important to note that the particle size distribution is divided into bins, each of which is treated as a separate phase. The mathematical model, which has been implemented using openFOAM (see Fig. B.2), an open-source CFD code, is discussed in the appendices. The governing equations are solved sequentially using the Finite-Volume Method (FVM). Accordingly, the equations are integrated at each computational cell, yielding discretized equations for each quantity.

### 2.1. Experiments

Gillard et al. (2019) study DSM-generated turbidity flows, where the flocculation process is quantified experimentally. To our knowledge, the flocculation parameters that we believe to play the largest role in controlling aggregation and breakup processes, i.e.  $d_f$  and  $E_b$ , have not been calibrated for CCZ-type sediment. The exact values and sensitivity of these parameters therefore remain unknown, which is why we use the experimental results of Gillard et al. (2019) to calibrate the parameters in Eq. (B.17) to predict the mixture as accurately as possible. It is worth noting that despite Gillard et al. (2019)'s extensive research on real CCZ sediment, an important limitation of their study is the absence of in-situ CCZ water. The use of natural water is crucial in understanding the aggregation process in CCZ environments. As a result, the experimental work in Gillard et al. (2019) did not fully consider the impact of key factors such as extracellular polymeric substances (EPS) and bacteria present in real CCZ water on the aggregation of particles. However, to the best of our knowledge, this is still the only work in the literature that has detailed laboratory results for CCZ sediment.

Gillard et al. (2019) used a horizontal Couette reactor (Fig. 1) to create a homogeneous shear rate. The reactor consists of a fixed inner cylinder and a rotating outer cylinder with a 2 cm wide annular space between the walls and a total working volume of 1.7 litres. The shear flow is generated by rotating the outer cylinder. The floc aggregation process is observed over time using a camera, as the outer chamber is made of transparent acrylic glass. The mixture is tracked during each experimental run.

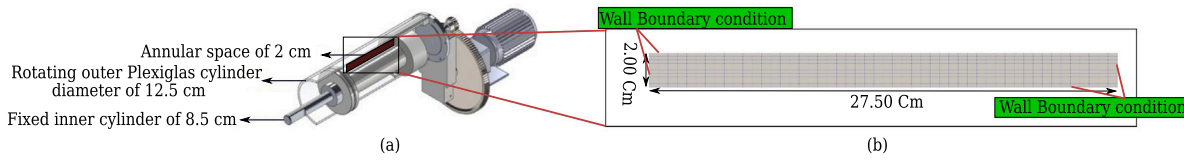


Fig. 1. (a) Couette reactor setup. (b) The 2D mesh used in numerical runs.

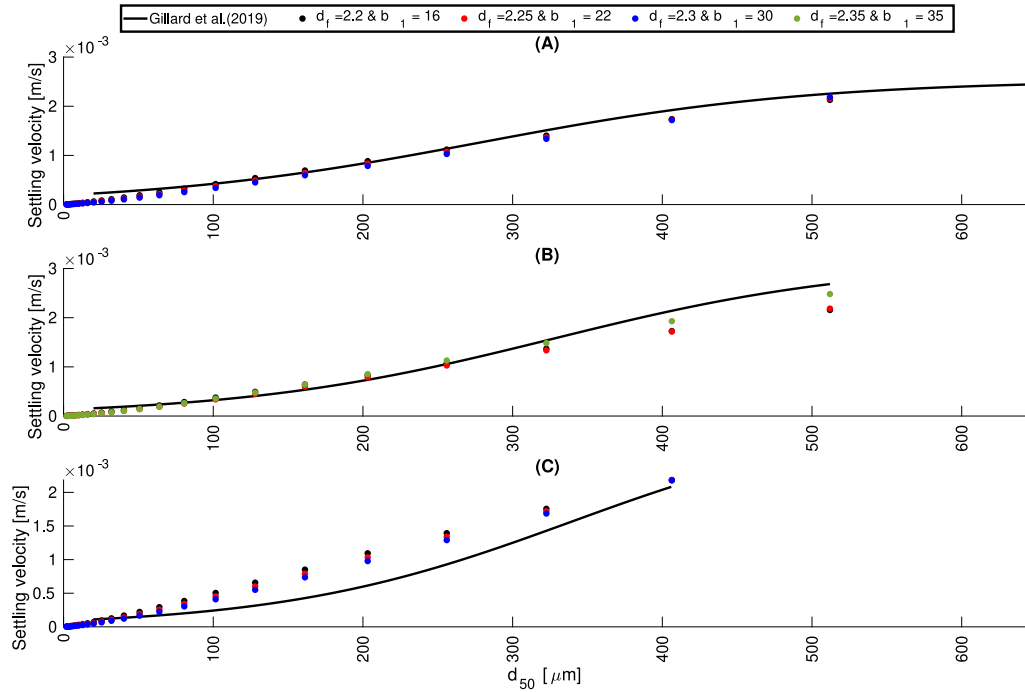


Fig. 2. Calibration of the modelled settling velocity  $u_{sr}$  using the experimental results of Gillard et al. (2019). (A): calibration process for 500 mg/l and 10.4  $s^{-1}$ . (B): calibration process for 175 mg/l and 5.7  $s^{-1}$ . (C): calibration process for 105 mg/l and 2.4  $s^{-1}$ .

## 2.2. Numerical domain

A 2D mesh is created using OpenFOAM's block-Mesh utility to represent a horizontal slice of the Couette reactor's working volume (see Fig. 1). The mesh is 25.7 cm long and 2 cm high. All sides are assigned a Wall Boundary Condition (B.C), with a no-slip B.C assigned to velocity, a zero gradient assigned to pressure, wall functions assigned to  $k$  and epsilon, and a zero gradient assigned to  $\alpha_k$ .

In the model, turbulence inside the Couette reactor is kept constant due to the constant angular velocity created by the rotation of the outer wall, resulting in a constant shear rate  $G$  throughout an experimental run. Despite the constant turbulence in the experiments, the turbulence model (Eqs. (A.7) and (A.8)) is not activated during the simulation, as constant values are assigned to  $k$  and  $\epsilon$ , which are used to calculate  $\Gamma$  in Eq. (B.18) and  $v_m'$  in Eq. (A.2). The current study focuses solely on calibrating the most effective flocculation parameters in the RHS of Eq. (B.17).

The shear rate in an experimental run is used to calculate the value of  $\epsilon$  for each case by using the equation  $G = (\epsilon/\nu_m)^{0.5}$ . The turbulence length scale relation is then used to determine  $k$  as follows:

$$\epsilon = \frac{C_\mu^{0.75} k^{1.5}}{L}, \quad (1)$$

where  $L$  is taken as 0.02 m, the distance between the outer and inner walls of the reactor. The volumetric concentration  $\alpha_k$  of each phase is then averaged over the entire domain, leading to the determination of  $d_{50}$ .

## 2.3. Settling velocity calibration

It is important to note that of the seven flocculation parameters  $E_b$ ,  $d_2$ ,  $C_b$ ,  $d_f$ ,  $b_1$ ,  $b_2$ , only three  $d_f$ ,  $b_1$ , and  $E_b$ , (see the appendices for the definition of these parameters), are considered for calibration, as they have been found to have a high impact on the results, while the other four have been found to have only a slight impact.

As mentioned in the work of Ferguson and Church (2004), the values of  $b_1$  range from 18 to 24 and  $b_2$  range from 1 to 1.2 for sand. However, when dealing with flocculation, the fractal dimension  $d_f$  plays a crucial role as it describes the space-filling ability of real flocs. According to Strom and Keyvani (2011), the settling velocity changes with the variation of the fractal dimension. Therefore, we determine the particle shape parameter  $b_1$  corresponding to the tested fractal dimension by calibrating the measured settling velocity of Gillard et al. (2019) to the results of Eq. (C.3), using the specific fractal dimension being tested. This allows us to determine the optimal value of  $b_1$ , taking into account that we found that the value of  $b_2$  did not have a significant impact on the results and is thus kept constant at 1.5.

Gillard et al. (2019) conducted settling velocity measurements which are used to calibrate parameters  $b_1$  and  $b_2$  in Eq. (C.3). The particle sizes varied from an initial  $d_{50} = 20 \mu m$  to the maximum floc size in each case. The results from Eq. (C.3) are compared to the experimental results and the case-dependent empirical formulas from Gillard et al. (2019) are used.

Fig. 2 shows the calibration of parameter  $b_1$  using different values of  $d_f$ . In Section 2.4, the fractal dimension for each of the 3 test cases is

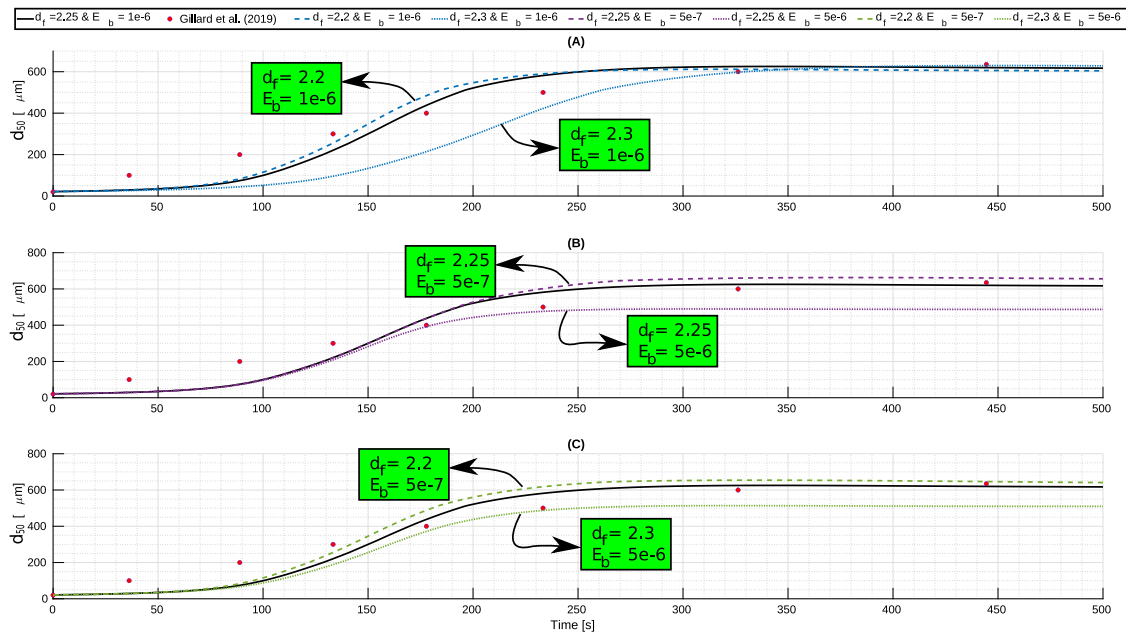


Fig. 3. Calibration process in case of 500 mg/l mass concentration and  $10.4 \text{ s}^{-1}$  shear rate. All 3 figures show the development of  $d_{50}$  over time. (A) represents the sensitivity of the fractal dimension  $d_f$  on the numerical results, where the breakage coefficient  $E_b = 1 \times 10^{-6}$  is constant. (B) represents the sensitivity of the breakage coefficient, where the  $d_f = 2.25$  is constant. (C) represents the sensitivity of both parameters  $d_f$  and  $E_b$  on the development of  $d_{50}$ .

determined. The settling velocity measurements in the figure are case-specific. The results from Eq. (C.3) agree well with the experimental results.

However, there is some discrepancy between the measured and calculated settling velocities, particularly in the low-shear rate conditions and for small particle sizes. This divergence may be attributed to several factors including:

- The uncertainty about the primary particle size  $d_2$ .
- Assuming a constant fractal dimension for the entire size range of particles.
- As a result, changes in fractal dimension can also affect the particle shape coefficient  $b_1$ , which can ultimately impact the calculations.

#### 2.4. Calibration results

The calibration set consists of three distinct cases, each characterized by a unique combination of mass concentration and shear rate. The concentrations tested are 500, 175, and 105 mg/l, paired with shear rates of 10.4, 5.7, and  $2.4 \text{ s}^{-1}$  respectively. These varied conditions allow for a comprehensive evaluation of flocculation behaviour. Our observations indicate that the fractal dimension and breakage coefficient play a crucial role in determining the flocculation source terms, highlighting their significance in this process. In each case, the values that fit closest to the experimental results are used as reference values, with the side note that they are determined through trial and error. The best fit for each case is represented graphically as a solid black line in Figs. 3, 4, and 5. To determine the sensitivity of the parameters, additional numerical runs are performed by varying the values of either  $d_f$  or  $E_b$ , or both. These additional experiments are depicted in (A) for  $d_f$  only, (B) for  $E_b$  only, and (C) for both  $d_f$  and  $E_b$  combined, in Figs. 3, 4, and 5.

The results of the numerical simulations and experiments are compared and a good agreement is found for a range of fractal dimension and breakage coefficient values. The best fit for each case is shown as a solid black line in Figs. 3–5. The values of  $d_f$  and  $E_b$  are relatively similar from case to case, which is anticipated as they represent the same sediment. These results provide us with the necessary confidence to

use these values in real-world applications (as discussed in Section 3). Given the complexity and uncertainty associated with these parameters, it is deemed acceptable to use any value within the specified range to a certain extent.

In all cases, the solid black lines deviate from the experimental observations at the start of the simulation, but they begin to match more closely soon after. The deviation in the numerical prediction of  $d_{50}$  is higher when  $E_b$  is changed compared to when  $d_f$  is changed. The undervaluation of  $d_{50}$  increases as  $E_b$  decreases and vice versa. The deviation caused by changing  $d_f$  is more prominent at the start of the numerical simulation. It is clear that as the initial concentration and shear rate decrease, the sensitivity of  $E_b$  increases (as seen in B and C in Fig. 5), leading to greater inaccuracies in the prediction of  $d_{50}$ . It could be that the overall deviation occurs due to:

1. The uncertainty in the initial particle size distribution (PSD) can have an impact on the calculation of the initial phase concentration ( $\alpha_k$ ), particularly during the early stages of a numerical run.
2. Only a small number of fractions are used.
3. The uncertainty of the constant values assigned to different parameters such as  $d_f$ ,  $E_b$  and  $b_1$ .
4. The assumption of the primary particle size being  $d_2 = 2 \mu\text{m}$ .
5. The shear rates explored in the study are relatively low, which could allow sediment particles to settle during the experiment, potentially impacting the accuracy of the measurements.
6. The possibility that the source terms of the PBE are only approximate.

It is critical to conduct a sensitivity analysis of parameters such as  $d_f$  and  $E_b$  before starting a numerical investigation, as improper estimation of these values may lead to significant over- or under-estimation of  $d_{50}$ , as demonstrated in (C) of Figs. 3–5. Fortunately, the ranges of the parameters for the three cases investigated in this study, namely  $2.25 \leq d_f \leq 2.3$  and  $2.5 \times 10^{-6} \leq E_b \leq 9 \times 10^{-5}$ , are considered valid for use in CCZ sediment case studies. However, it is important to conduct a sensitivity analysis for each individual sediment type prior to applying the numerical model.

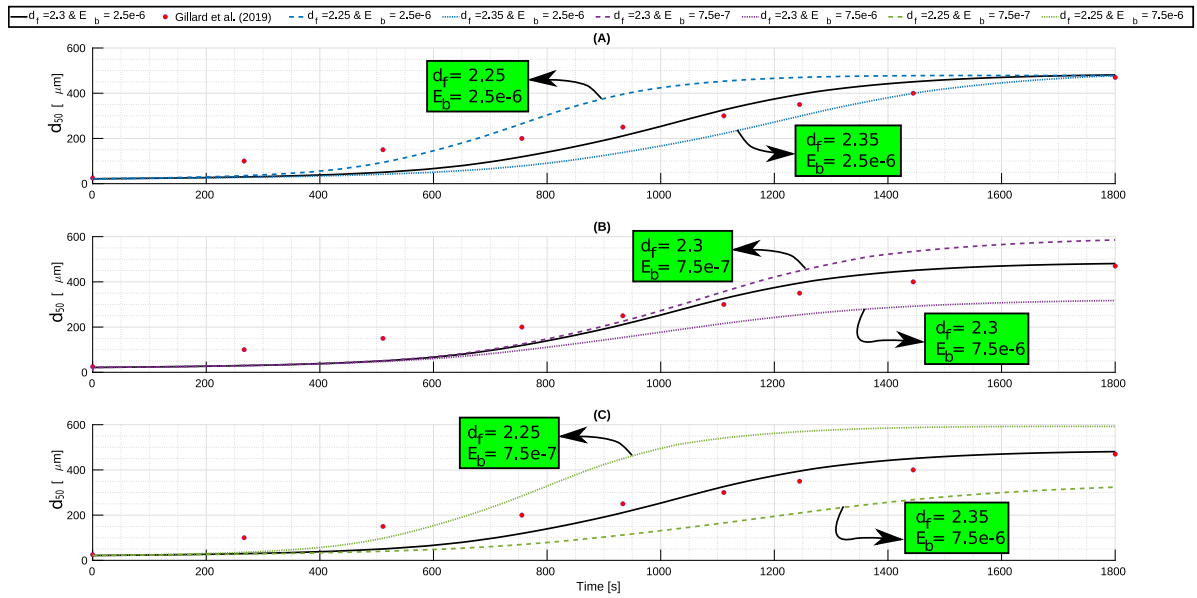


Fig. 4. Calibration process for 175 mg/l mass concentration and  $5.7 \text{ s}^{-1}$  shear rate. All 3 figures show the development of  $d_{50}$  over time. (A) represents the sensitivity of the fractal dimension  $d_f$  on the numerical results, where the breakage coefficient  $E_b = 2.5 \times 10^{-6}$  is constant. (B) represents the sensitivity of the breakage coefficient, where the  $d_f = 2.3$  is constant. (C) represents the sensitivity of both parameters  $d_f$  and  $E_b$  on the development of  $d_{50}$ .

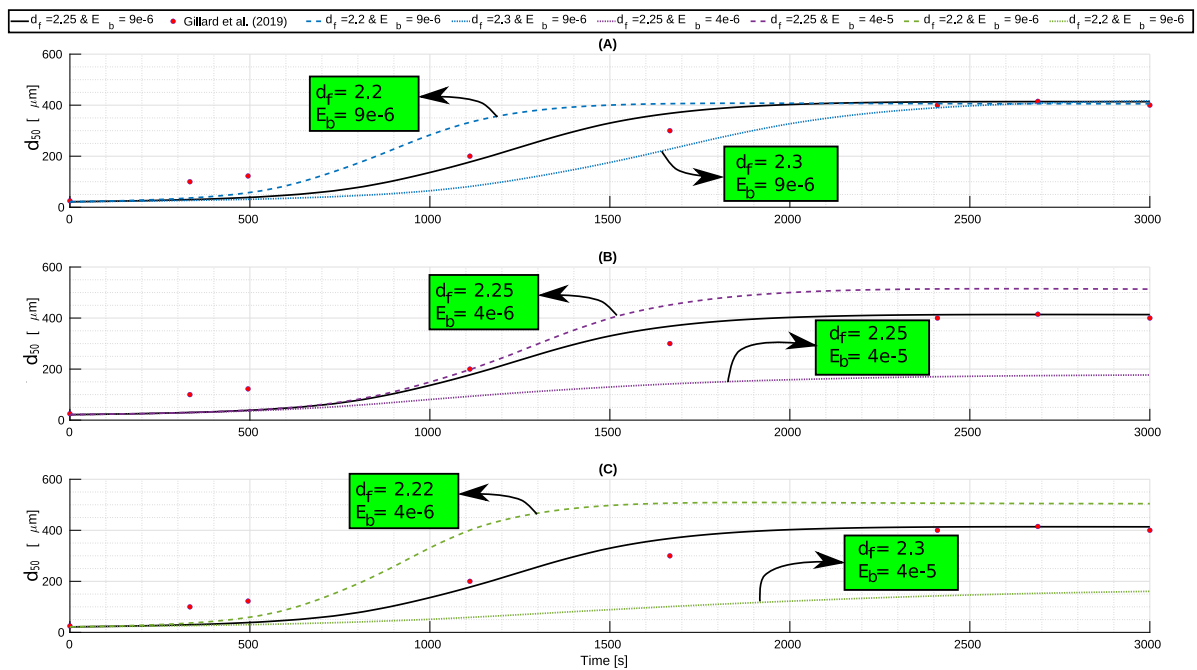


Fig. 5. Calibration process in case of 105 mg/l mass concentration and  $2.4 \text{ s}^{-1}$  shear rate. All 3 figures show the development of  $d_{50}$  over time. (A) represents the sensitivity of the fractal dimension  $d_f$  on the numerical results, where the breakage coefficient  $E_b = 9 \times 10^{-6}$  is constant. (B) represents the sensitivity of the breakage coefficient, where the  $d_f = 2.25$  is constant. (C) represents the sensitivity of both parameters  $d_f$  and  $E_b$  on the development of  $d_{50}$ .

### 3. Case studies

The multi-phase-drift-flux model has been previously validated through experimental studies conducted by Elerian et al. (2022). The results of our analysis have demonstrated that the flocculation source terms of the model are effective in predicting the median grain size  $d_{50}$  of a water–sediment mixture. With this validation and calibration, we can now move forward to explore the impact of flocculation on turbidity current dispersion in the near-field region, which will be the focus of the next section.

#### 3.1. Numerical domain

As a PNMT travels along the seabed, it creates a highly turbulent region in its wake. The sediment particles generated by the PNMT are then subjected to high levels of mixing and increased chances of particle collisions, which can lead to either the aggregation of particles or the breakup of newly formed flocs. With the aim of investigating the effects of flocculation in the near-field region, we will be using the model described in appendices to conduct two main simulations as follows:

1. With flocculation,

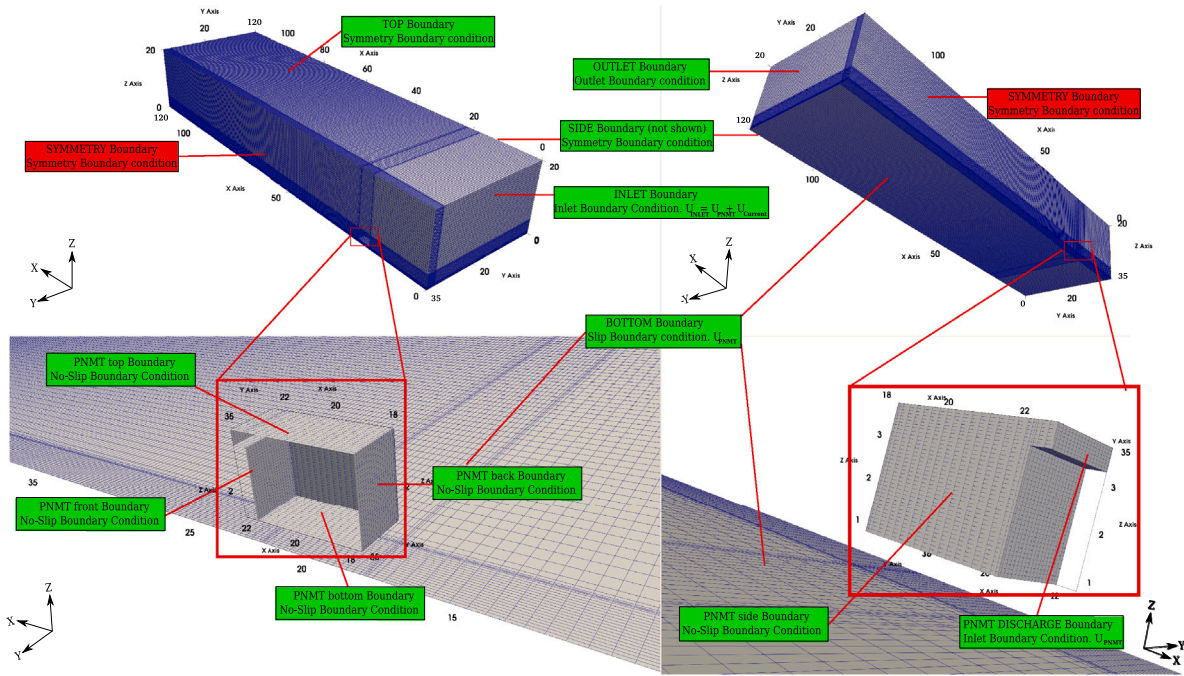


Fig. 6. Geometry used in all numerical simulations with the name of the relevant B.C. The top figures depict half of the domain, utilizing symmetry B.C as indicated by the red tag, while the bottom figures show the geometry for the PNMT. The unrepresented half of the domain is mirrored along the ZX plane for post-processing analysis. The flow direction is in the positive X direction with a positive discharge.

2. Without flocculation, i.e. the 6 flocculation terms in Eq. (B.17) = 0.

Additionally, we have established in Section 2.4 that the flocculation behaviour is highly dependent on  $d_f$  and  $E_b$ . To further understand the impact of these parameters on the near-field region, we conduct four additional simulations, each varying the values of  $d_f$  and  $E_b$  by  $\pm 0.5$  and  $\pm 5 \times 10^{-7}$ , respectively, from the values used in Run 1. The complete details of all numerical simulations performed can be found in Table 1. Runs 1 and 2 are the main simulations, with one examining the effects of flocculation and the other without, while Runs 3–6 are designed to assess the sensitivity of the flocculation parameters as outlined in Section 3.5.

It is further to be noted that for the no-flocculation case (Run 2), a non-cohesive sediment (e.g. sand) should be used, so the simulation should start with the PSD of the 8 MUC location (same initial spectrum of the flocculation case, see Fig. C.1), considering it as sand. The settling velocity for the no-flocculation case is calculated using the Ferguson formula (Eq. (C.1)) for the sand fractions throughout the simulation. However, using this approach for comparison with the flocculation case is invalid as the latter uses Eq. (C.3). Therefore, while comparing the results, not only the phase transition will be the changing parameter but also the settling velocity, which can affect the conclusions regarding the observed difference in the numerical results. Consequently, this can affect the conclusions regarding whether the observed difference in the numerical results is due to using different settling velocity formulas or because of the phase transitions. Therefore, we unify the settling velocity calculations using only Eq. (C.3) for both cases with a  $d_f = 2.25$ , allowing the phase transition to be the only changed parameter. In other words, when we use the term “no-flocculation” case, we are referring to a scenario where there is no phase transition occurring (i.e. the particle size distribution is only affected by transport mechanisms and not the phase transition). In this case, we assume that the settling velocity of the particles is calculated in the same way as in the flocculation case. By making this assumption, we can isolate the effect of the phase transition on the settling behaviour of the particles and better understand flocculation impact.

Table 1  
The values of  $d_f$  and  $E_b$  used in the numerical runs.

Runs	1	2	3	4	5	6
$d_f$	2.25	2.25	2.2	2.3	2.25	2.25
$E_b$	5e-6	0	5e-6	5e-6	1e-7	1e-6

The computational domain, with dimensions of 20 m in height, 35 m in width, and 120 m in length, is depicted in Fig. 6. The length of the domain, 120 m, is selected to accommodate the flocculation process, as it requires substantial time and length scales to occur effectively. Preliminary simulations, not depicted, indicated that a sufficient distance should be maintained between the INLET, SIDE, TOP, and PNMT boundaries to prevent pressure disturbance between the boundaries. As depicted in Fig. 6, the positioning of the PNMT back is set at 18 m from the INLET boundary, the side of the PNMT is placed at 34 m from the SIDE boundary, and the PNMT top is positioned at 16.5 m from the TOP boundary to ensure the aforementioned distance requirements are met, as established by the preliminary simulations. As shown in Fig. 6, the PNMT geometry is kept simple, as the main objective of the simulation is not to optimize PNMT geometry, but rather to study the flocculation process. Additionally, it is important to note that our study does not take into account the effects of any aggregation or breakage that may occur within the PNMT, keeping in mind that the collection process is highly turbulent due to the high velocity jets involved, which may impact the behaviour of particles (Alhaddad and Helmons, 2023). The background oceanic current is assumed to be 0.1 m/s, as reported in (GSR, 2018). As this is a moving source problem, the PNMT is considered the reference frame, with a forward speed of 0.5 m/s, which is equal and opposite in direction to the mixture discharge velocity, as reported in (GSR, 2018; Gillard and Thomsen, 2019). It is worth mentioning that the PNMT moves in the negative X direction. Our hypothesis is that discharging the mixture at a velocity equal to the forward speed of the PNMT would result in an immediate transition to the negative buoyancy phase, minimizing dispersion due to the expected lower velocity of the generated turbidity current. It is important to note that the focus of this study is not to examine

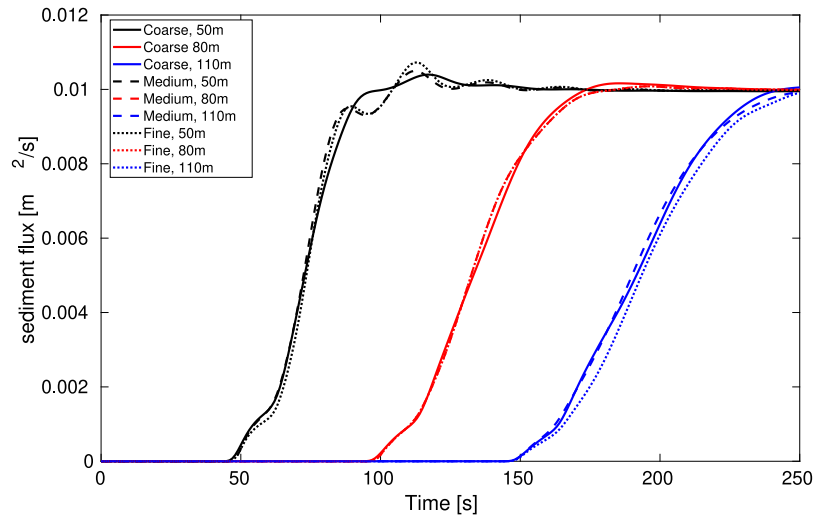


Fig. 7. Comparison of sediment flux in coarse, medium and fine mesh. In each case, three x-normal slices are considered at 50 m, 80 m and 110 m.

Table 2

Boundary condition set up at different positions for all variables.

Boundaries	U [m/s]	$P_{pgh}$ [pa]	$\alpha_t$ [%]	k $\times 10^{-4}$ [m <sup>2</sup> /s <sup>2</sup> ]	$\epsilon$ [ $\times 10^{-6}$ ] [m <sup>2</sup> /s <sup>3</sup> ]
INLET	0.5	zero gradient	0	1.5	1.5
OUTLET	–	0	zero gradient	zero gradient	zero gradient
TOP	zero gradient	zero gradient	zero gradient	zero gradient	zero gradient
BOTTOM	0.5	zero gradient	zero gradient	0	0
SIDE	zero gradient	zero gradient	zero gradient	zero gradient	zero gradient
SYMMETRY	symmetry	symmetry	symmetry	symmetry	symmetry
All PNMT	0	zero gradient	zero gradient	Wall	Wall
PNMT	0.6	zero gradient	1%	Function	Function
DISCHARGE					

the impact of varying discharge velocities or PNMT speeds, but to investigate the effects of flocculation in the near-field region. Given that the PNMT serves as the reference frame, the bottom wall of the PNMT has a speed equal to the forward speed of the PNMT, creating a boundary condition conflict between the bottom of the PNMT (no-slip boundary,  $U = 0$  m/s) and the BOTTOM boundary (slip boundary,  $U = 0.5$  m/s). However, it is assumed that the sediment disturbance caused by the PNMT tracks would be negligible compared to the discharge source from the PNMT. To account for this, a 0.8 m empty space is maintained between the boundaries, as seen in the right-bottom figure in Fig. 6.

Leveraging the symmetry of the problem, only half of the domain is solved and the result is mirrored across the XZ plane during post-processing, effectively reducing the computing power required by half. Table 2 and Fig. 6 show the boundary conditions for various variables. The simulation is run for 250 s to ensure a steady-state case for the turbid flow, even though a simulation time of 200 s is sufficient for the PNMT to traverse the 100 m domain length. A single run takes about 5 days on 64 cores of the Delft-Blue supercomputer (Delft High Performance Computing Centre (DHPC), 2022).

### 3.2. Mesh structure and sensitivity

The computational mesh consists of approximately 3.5 million cells. To capture the density difference in front of the PNMT, grid clustering with increased resolution is applied in the positive x, y, and z directions. The cells in the first 4 m have a height of 3 cm, length of 20 cm, and width of 10 cm, while those in other regions are 50 cm in all directions. The cell size around the PMNT gradually increases with a growth rate of 1.003 in the normal direction of each PNMT boundary.

In addition to the coarse mesh described above, two other meshes, the medium and fine, are considered to evaluate the solution's dependence on the number of cells. The medium mesh has approximately 6.5 million cells and represents a 1.25-fold increase, while the fine mesh has approximately 11.5 million cells and represents a 1.5-fold increase in cells compared to the coarse mesh. The sediment flux, represented by  $\alpha_t \times U_{m,x} \times A$ , is chosen as the key metric in this study. Our analysis of the sediment flux over time in three cross-sections of 50 m, 80 m and 110 m, as shown in Fig. 7, revealed minimal variations among the meshes. For this reason the coarsest mesh is used for this study.

### 3.3. Flocculation nature

To understand the behaviour of turbid flows in the near-field region, we compare cases with and without flocculation. This comparison will highlight the significance of flocculation and provide insight into whether it can play a role in reducing the turbidity flows caused by DSM. To do so, we monitor the sediment flux  $\alpha_t$  and the fractional fluxes  $\alpha_2$ ,  $\alpha_{22}$  and  $\alpha_{28}$  through three cross-sections (yz plane) at 50 m, 80 m, and 110 m, as shown in Fig. 8. The data is collected from run 1 and 2. The three fractions,  $\alpha_2$ ,  $\alpha_{22}$  and  $\alpha_{28}$ , represent particle sizes of  $d_2 = 2 \mu\text{m}$ ,  $d_{22} = 256 \mu\text{m}$  and  $d_{28} = 812.7 \mu\text{m}$ . These fractions are carefully chosen as they represent the smallest and largest particles ( $d_2$ ,  $d_{22}$ ) in the initial particle size distribution (PSD), as well as the largest possible aggregate ( $d_{28}$ ), as illustrated in Fig. C.1.

While there is little variation in the total sediment flux between the two runs, as shown in Fig. 8 (A), a notable difference can be observed in the fraction fluxes in (B), (C), and (D). In the case of flocculation, the fraction flux (Fig. 8 (B)) is significantly lower compared to the no-floc case, primarily due to aggregation processes that cause particles

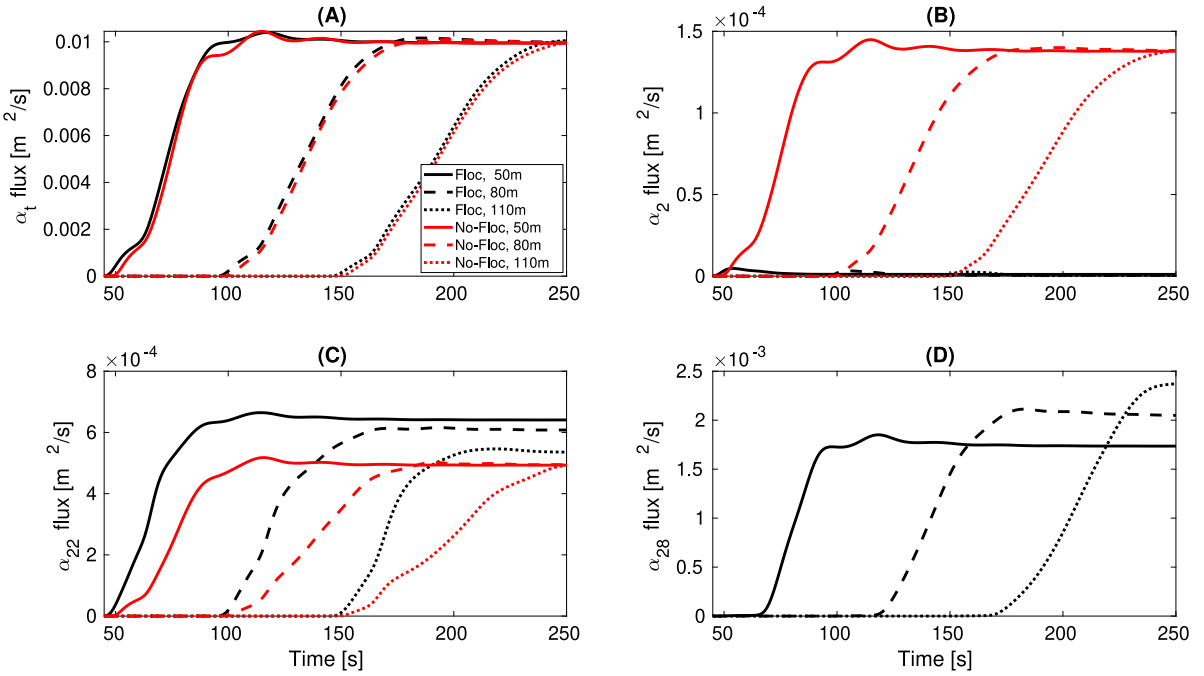


Fig. 8. Fraction fluxes across the three x-normal slices, slice1 at 50 m, slice2 at 80 m and slice3 at 110 m. (A)  $\alpha_t$  flux, (B)  $\alpha_2$  flux, (C)  $\alpha_{22}$  flux, (D)  $\alpha_{28}$  flux .

to transition from  $k = 2$  to higher-level phases. In contrast, without flocculation, the flux remains constant and unchanging across the cross-section as there are no aggregation mechanisms in play.

The aggregation process is further confirmed in Fig. 8 (C), where the steady-state flux decreases in the flocculation scenario from one cross-section to the next, a trend that is not present in the no-flocculation scenario. In the flocculation scenario, as seen in Fig. 8 (C), the steady-state flux is 23%, 19% and 8% lower in Sections 1, 2, and 3, respectively, compared to the no-flocculation scenario, indicating that the particles have transitioned to higher phases in the regions between these sections. The steady-state flux of  $\alpha_{28}$  shows an increase from one cross-section to the next, suggesting that lower fractions such as  $\alpha_{22}$  have undergone aggregation and progressed to the phase  $\alpha_{28}$ . The region behind the PNMT experiences a high shear rate due to its presence, leading to a higher rate of flocculation in cross-section 1 compared to the others. As the PNMT moves away, the particle aggregation rate gradually decreases.

In the case of  $\alpha_{28}$ , as shown in Fig. 8 (D), there is no no-flocculation scenario present throughout the simulation. Nevertheless, the development of the  $\alpha_{28}$  flux can be presented to demonstrate that finer phases undergo aggregation, resulting in an increase in the steady-state flux.

### 3.4. Flocculation effect visualization

As the speed of the PNMT is equal to the discharge velocity, the discharged mixture immediately enters the negative buoyancy phase and then impacts the seabed, creating a turbidity current. Since the observed differences between the flocculation and no-flocculation scenarios are related to the sideways turbidity currents, we plot 4 z-normal sections – (xy) plane – for the volumetric concentration of the two runs at BOTTOM boundary and 1 m from the bottom boundary and 250 s (see Fig. 9). Moreover, the relative concentration difference is calculated, resulting in the top 2 figures in Fig. 10. Such that the relative concentration difference is calculated as follows:

$$\alpha_{t,difference} = \frac{\alpha_{t,no-floc} - \alpha_{t,floc}}{\alpha_{t,no-floc}} \quad (2)$$

This would result in a clearer visualization of the differences between the two cases, providing a more comprehensive understanding

of the extent to which flocculation affects the behaviour of turbidity currents. Furthermore, we plot 2 X-normal figures (bottom figures in Fig. 10) to clearly visualize the sediment distributions in the sideways turbidity current in both cases.

To explain the results, we must first introduce the structure of a turbidity current resulting from an instantaneous discharge. We consider a current that propagates to the right and left (along the y-axis) from the PNMT. At the beginning, a head forms and as it propagates, a body begins to appear. Over time, a tail starts to form. These are the three main structural regions of the side-way current, noting that not all sideways current shown herein have this structure.

In the flocculation and no-flocculation scenarios, the dispersion trend remains unchanged and the overall turbidity current forms a wedge shape in both cases. However, from the perspective of sediment distribution, there are significant differences between both cases, indicating that flocculation does have an effect in the near-field region. The regions most affected by flocculation are the head and body of a sideways turbidity current, particularly in cases where the current propagates for longer periods of time and the tail becomes visible. It is important to keep in mind that a sideways turbidity current that has only propagated for a shorter period of time is less likely to exhibit the tail region, which typically forms relatively close to the PNMT.

In the head region, the flocculation case has a higher volumetric concentration than the no-flocculation scenario. In the tail region, especially at section B-B in Fig. 10, the flocculation case has the highest sediment distribution in the lower region. There is also a slight flocculation effect in the body region, where in the no-flocculation scenario, the sediment remains in suspension, while the large flocs in the flocculation case have already settled.

These observed differences occur due to the migration of the fine fractions to the coarser fractions, forming new large fractions and enlarging existing ones. The large-formed flocs have relatively high settling velocities. For example, the  $u_{kr} = 0.00305$  for a floc size of  $d_{28} = 812.7 \mu\text{m}$  and density of  $\rho_{28} = 1018.23 \text{ kg/m}^3$ . This has two direct implications on the total sediment distribution: first, the elimination of fine particles with low settling velocities, and second, an increase in the total average settling velocity of the sediment as a whole. In contrast, this does not happen in the no-flocculation scenario, as it is clearly evident in Fig. 10 that at the top body region, the

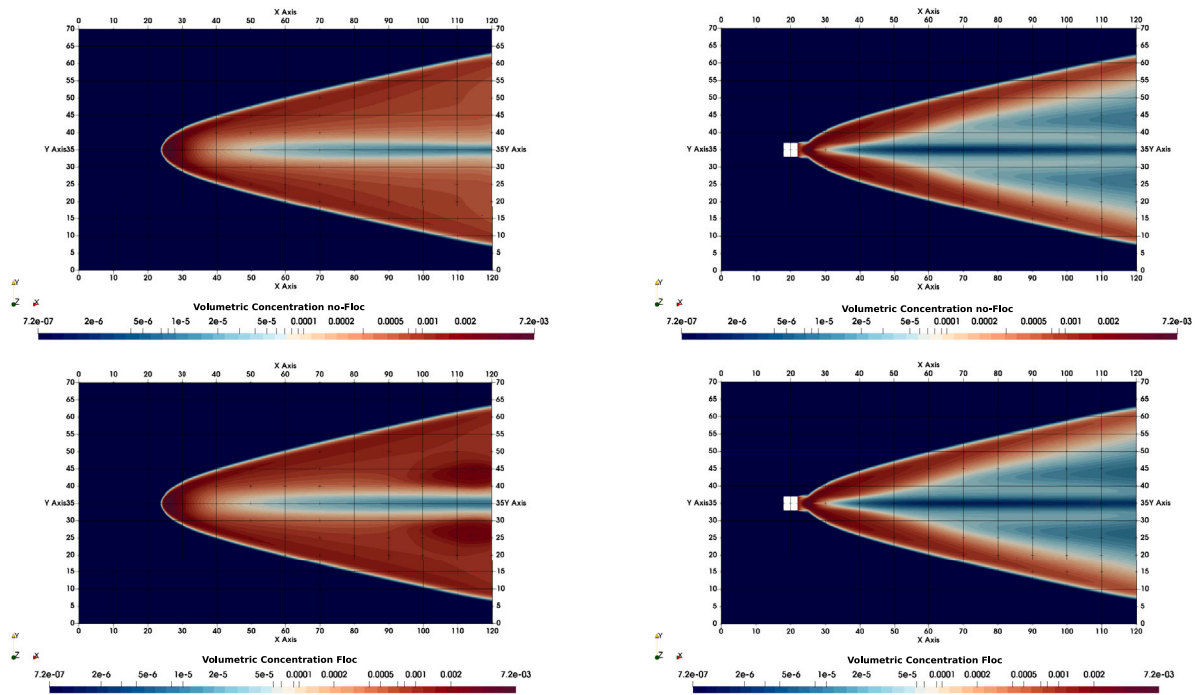


Fig. 9. Z-normal sections for the flocculation and no flocculation cases are taken at the BOTTOM boundary (left) and 1 m from the bottom (right). The top row shows the no-flocculation case, while the lower row shows the flocculation case.

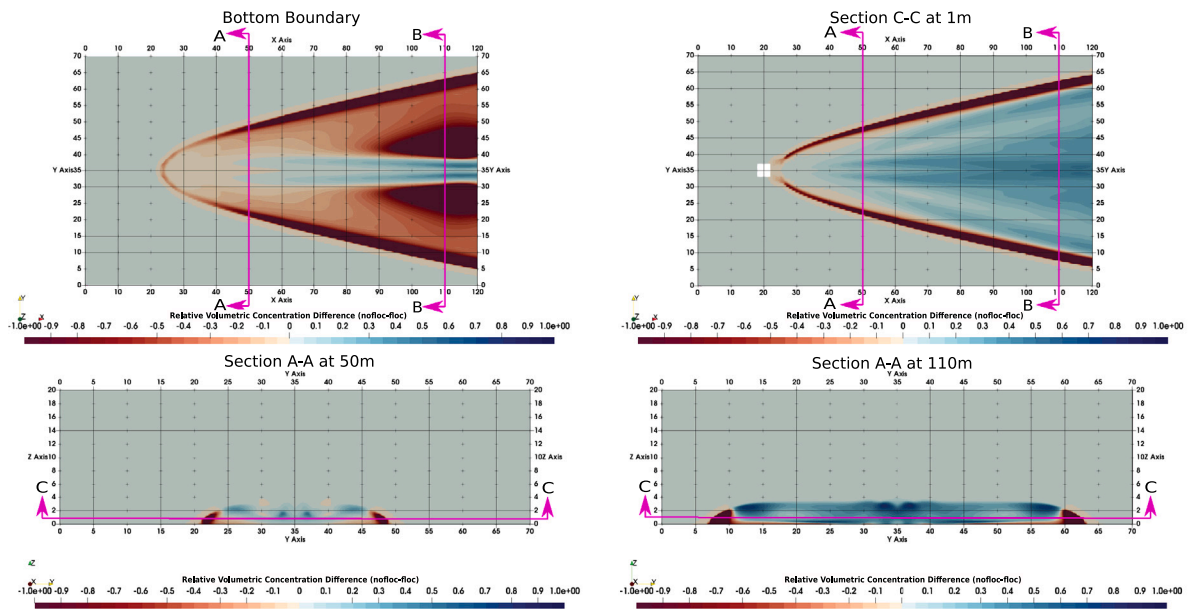


Fig. 10. Z and X normal sections show the relative differences between the flocculation and no-flocculation cases. The Z-normal sections are taken at the BOTTOM boundary (left) and 1 m from the bottom (right) which is section C-C, while the X-normal sections are taken at 50 m and 110 m from the INLET boundary.

no-flocculation case has a higher concentration than the flocculation scenario. This is because fine fractions with lower settling velocities are still in suspension. Despite the relatively large settling velocities of the large flocs, they remain in suspension in the head region due to the high mixing in this region.

To conclude,

1. In the near-field region, aggregation between particles is the dominant mechanism, leading to the formation of large particles

and the enlargement of existing ones. This results in the elimination of fine particles in the near-field region and generally an increase in the settling velocity of sediment particles.

2. As large particles settle out from the turbidity current, this reduces the concentration of the turbidity current, which subsequently creates an evident tail region of the side-ws current and reduce the amount of the transported sediment to the far-field.

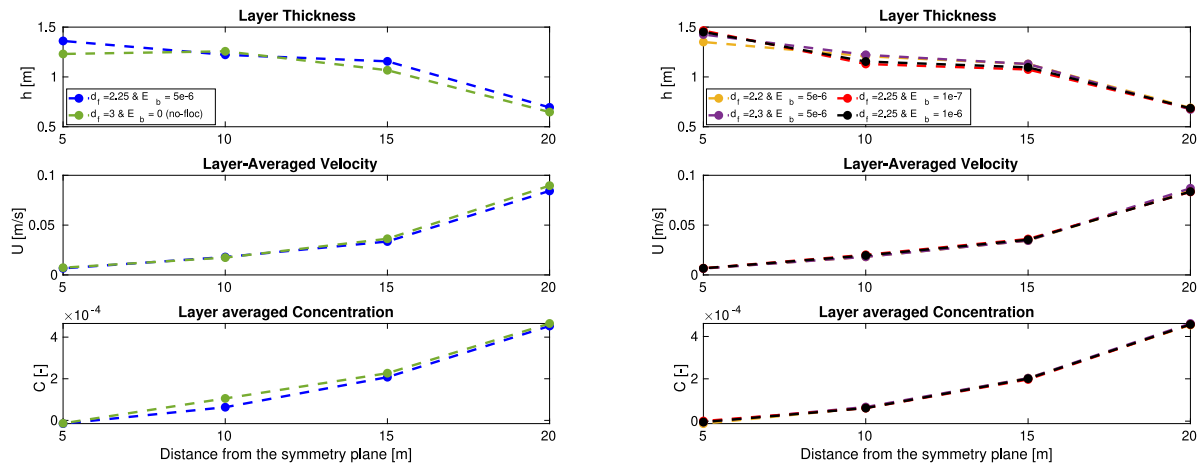


Fig. 11. Layer-averaged parameters of the sideways turbidity current. The flocculation scenarios are compared on the left, where the fractal dimension  $d_f$  and the breakage coefficient  $E_b$  are changing. The graphs on the right compare the flocculation scenario and no-flocculation scenario.

### 3.5. Layer averaged parameters

To further understand the impact of flocculation on turbidity currents, we conducted additional analysis focusing on the lateral flow in the region where differences are noted in the previous section (Section 3.4). Thus, we selected a point at 118 m on the X-axis, 100 m away from the front of the PNMT, located in the region where significant differences are observed. Four vertical concentration and velocity profiles, each 5 m in height, are taken along the run-out distance (Y-axis) at 15 m, 20 m, 25 m, and 30 m. The 35 m point is the SYMMETRY boundary and 0 is the SIDE boundary (Fig. 6). The layer-averaged parameters are calculated using the following equations:

$$Uh = \int_0^{z_\infty} u_y dz, \tag{3}$$

$$U^2h = \int_0^{z_\infty} u_y^2 dz, \tag{4}$$

$$UhC = \int_0^{z_\infty} \alpha_y u_y dz, \tag{5}$$

where  $z$  [m] is the upward normal coordinate,  $h$  [m] is the height of the current,  $U$  [m/s] is the layer-averaged velocity,  $C$  [-] is the layer-averaged concentration and  $u$  [m/s] is the local velocity and  $z$  is the vertical coordinate. Fig. 11 shows the layer averaged parameters for both the flocculation and no-flocculation scenarios. We also examined the other 4 scenarios, runs 3–6 (Table 1), in order to assess the sensitivity of the flocculation parameters.

In general, adjusting flocculation parameters  $d_f$  and  $E_b$  has a slight effect on the determination of the flocculation process, see the leftmost figures in Fig. 11. This, however, does not affect the main comparison between the no-flocculation scenario (Run 2) and the flocculation scenario (Run 1), since hardly any differences are observed with respect to layer-averaged velocity and concentration in Runs 3–6, unlike the difference observed between the two cases (Runs 1,2), which can be spotted immediately (right figures in Fig. 11), implying that only the flocculation process is responsible for the observed differences between Runs 1,2. In other words, changing flocculation parameters at this level of scale, i.e. the near-field region, does not have a major impact on flocculation. We can now proceed with our main investigation: determining the effect of flocculation by comparing Runs 1,2.

In the no-flocculation scenario, the layer-averaged velocity in regions far apart from the middle region is almost 6% higher than in the flocculation scenario. Moreover, while flocculation does occur, the turbidity current has a lower layer-averaged concentration, resulting in a higher layer-averaged thickness in the flocculation scenario than in the no-flocculation scenario. As the current propagates along the run-out distance, particles aggregate and particle size increases, with the

freshly formed flocs exhibiting an increased settling velocity. Therefore, in the no-flocculation scenario, sediment particles are still in suspension, providing the current with extra buoyancy force that is not present in the flocculation scenario. It is worth mentioning here that buoyancy force is one of the main driving forces of a turbidity current, which is why differences are observed between the layer-averaged parameters.

### 3.6. Discussion

While flocculation is active and the sideways turbidity current propagates, the current is expected to lose its momentum quickly due to the settling of particles in the body and the tail parts, implying that lower amount of sediment will be available for the passive transport phase, which comes directly after the turbidity current phase. In the passive transport phase, the sediment is transported based on the background current, ambient turbulence and topography (Ouillon et al., 2021). This is more likely to happen in the far-field region. Thus the current work proves that there should be enough attention to optimize the PNMT including the discharge conditions to promote flocculation in the near-field region. Despite the slight effect of the flocculation in the near-field region, we believe according to the insights that are gained from the previous sections that flocculation will definitely plays a major role in the far-field region.

Although the aforementioned results present an understanding of the effects of flocculation in the near-field region, flocculation might be under/overestimated due to the PNMT design considered here, which is simple and does not represent a real PNMT design. We know that the wake region is highly dependent on PNMT geometry and different estimated shear rates will have a different effect on flocculation dynamics. Studying the effect of PNMT geometry on flocculation dynamics can provide unique insights into the most favourable conditions for flocculation in the near-field region. This, in turn, will improve the settling potential of flocs in the near-field regions, which will have a positive effect on the far-field region.

If flocculation results in a low degree of polydispersity among the sediment within the mixture, it could lead to the current dissipating more quickly, as demonstrated by Harris et al. (2002), who showed that any level of polydispersity can add to the run-out length compared to a monodisperse current with an equivalent settling velocity. In addition, they found that faster settling particles, or “flocs”, contribute to shorter run-out distances. Therefore, considering both the effects of a low degree of polydispersity and faster settling flocs, a current with flocculation would likely dissipate more quickly than one with no or lower levels of flocculation.

The results of the systematic comparison between flocculation and no-flocculation presented in this study suggest that flocculation is likely

to occur in the near-field region immediately following discharge. The aggregation of sediment particles has a limited impact on the behaviour of turbidity currents in the near-field, with the flocs within the current showing a high propensity for settling. Our results indicate that flocculation does not significantly affect the behaviour of turbidity currents generated by DSM in the near-field region. However, it is expected to have a notable and distinguishable impact in the far-field region.

#### 4. Conclusions

This study sought to investigate the effect of flocculation in the turbidity flows generated by polymetallic nodule mining. The numerical evaluation demonstrates that sediment readily flocculates to form large particles that will settle as soon as the turbidity current subsides enough to allow this to happen, this process is likely occurring in the far-field region. The flocs are rapidly forming due to the turbulence caused by the PNMT, particularly in the region close to the PNMT. Furthermore, it is evident from the numerical work that the aggregation mechanism is more dominant than the break-up mechanism. The effects of flocculation can be observed in the near-field region, but they are limited to have a significant impact on the turbidity current in the vicinity of the PNMT.

Drift-Flux modelling coupled with the Population Balance Equation serves as an acceptable tool for modelling the hydrodynamics of water-sediment mixtures, which are present in DSM activities. Therefore, different discharge scenarios need to be investigated in order to gain more insight into the effect of flocculation in the near-field region. However, it is crucial to arrive at a proper estimation of the fractal dimension and breakup coefficient first. Moreover, the design of PNMTs may be adapted to foster conditions that are more favourable for flocculation. It is worth noting that turbulence modelling is crucial in flocculation modelling, since the shear rate is directly related to the flocculation source terms. Therefore, better representation of the turbulence in the wake region is recommended, since the buoyant  $k-\epsilon$  model still lacks 2 important kinetic energy damping mechanisms: the turbulence flux of momentum in the vertical direction and the extra vertical mixing between the flow layers due to the particles, i.e., the turbulent wake resulting from particle deposition in the vertical direction. It is also important to assess the sensitivity of these two damping mechanisms on the shear rate, which, in turn, is responsible for the collision/breakage dynamics of the flocs. Using spatial averaging rather than time averaging to estimate turbulence characteristics might help improve the representation of turbulence and therefore flocculation, but the amount of computing power required to do so must be taken into consideration.

With the intention of simplifying our current analysis, we omit the consideration of the front collection process. However, this aspect could play a crucial role in affecting the particle's fate through its effect on the flocculation process, from the moment of collection to the moment of discharge. To enhance the accuracy of our findings, it would be wise to conduct a separate study to estimate the particle size distribution and the primary particle size at the moment of discharge. This would provide a more dependable representation of the results.

Another limitation of our calibration process is the limited availability of detailed experimental data on CCZ sediment. So far, only one study in the literature, (Gillard et al., 2019), has investigated this topic in depth. Therefore, the calibration is based on a single data set and may not be applicable to other studies. In addition, these experimental results did not use in-situ seawater, which is a crucial factor in any flocculation research. To improve the robustness of our method, further calibration should be conducted using additional data sets using in-situ water samples to establish appropriate values for the flocculation parameters.

#### CRedit authorship contribution statement

**Mohamed Elerian:** Conceptualization, Methodology, Writing – original draft, Visualization, Investigation, Software, Formal analysis. **Ziyang Huang:** Software. **Cees van Rhee:** Conceptualization, Methodology, Writing – review & editing, Funding acquisition. **Rudy Helmons:** Conceptualization, Methodology, Formal analysis, Writing – review & editing, Funding acquisition.

#### Declaration of competing interest

The authors declare that they have no known competing financial interests or personal relationships that could have appeared to influence the work reported in this paper.

#### Data availability

Data will be made available on request

#### Acknowledgements

This study was conducted as a part of the Blue Harvesting project, supported by the European Union's EIT, EIT Raw Materials, and has received funding under Horizon Europe Partnership Agreement PA2021/EIT/EIT Raw Materials, GA2021 EIT RM, Specific Project Agreement 1813.8.

#### Appendix A. Drift-flux model

In this study, we adopt a continuum mixture approach, specifically the drift-flux model, to describe complex turbid flows. This approach involves solving the transport of individual sediment fractions separately and solving a single momentum equation for the mixture as a whole. Although this model assumes that sediment particles follow the carrier fluid, it does account for deposition. Compared to other continuum approaches such as the Euler–Euler model, the drift-flux model requires less computational power as it requires solving fewer equations. Drawing on the work of Goeree (2018), we present the main equations and closures that make up the drift-flux model. The mixture continuity equation can be expressed as follows:

$$\frac{\partial \rho_m \mathbf{u}_m}{\partial t} + \nabla \cdot \rho_m \mathbf{u}_m = 0, \quad (\text{A.1})$$

and the mixture momentum equation can be expressed as:

$$\frac{\partial \rho_m \mathbf{u}_m}{\partial t} + \nabla \cdot \rho_m \mathbf{u}_m \mathbf{u}_m = \nabla p_m + \nabla \cdot ((v_m + v'_m) \nabla \mathbf{u}_m) - \sum_{k=1}^n \alpha_k \rho_k \mathbf{u}_{km} \mathbf{u}_{km} + \rho_m \mathbf{g} + M_m, \quad (\text{A.2})$$

Where the subscripts  $k$  and  $m$  denote the phase  $k$  and the mixture  $m$ , respectively, with  $k = 1$  representing the liquid phase and  $\sum_{k=1}^n \alpha_k = 1$ .  $\rho_m$  is the mixture density, calculated as the sum of the product of each phase density and its volumetric concentration,  $p_m$  is the mixture pressure,  $\alpha_k$  is the volumetric concentration of phase  $k$ ,  $v_m$  is the kinematic viscosity of the mixture,  $v'_m$  is the eddy viscosity,  $M_m$  is an external source term,  $\mathbf{g}$  is the gravitational acceleration,  $\mathbf{u}_{km}$  is the relative velocity of phase  $k$  with respect to mixture  $m$ , and  $\mathbf{u}_m$  is the mixture velocity, defined as:

$$\mathbf{u}_m = \frac{1}{\rho_m} \sum_{k=1}^n \rho_k \alpha_k \mathbf{u}_k. \quad (\text{A.3})$$

The phase transport equation is introduced as follows:

$$\frac{\partial \alpha_k}{\partial t} + \nabla \cdot (\alpha_k \mathbf{u}_k) = \nabla \cdot \Gamma_i \nabla \alpha_k, \quad (\text{A.4})$$

$$\frac{\partial \alpha_k}{\partial t} + \nabla \cdot (\alpha_k (\mathbf{u}_m + \mathbf{u}_{km})) = \nabla \cdot \Gamma_i \nabla \alpha_k.$$

The Right Hand Side (RHS) of Eq. (A.4) is the turbulence diffusion, where  $\Gamma$  is the turbulence diffusion coefficient, which is a ratio between the eddy viscosity and Schmidt number. In this study the Schmidt number ( $S_{c_i}$ ), which is a turbulence property, is taken to be 1 since no universal value could be determined and the value of  $S_{c_i}$  is often assumed (Goeree, 2018). Eq. (A.4) is only solved for solid fractions  $k = 2$  to  $n$ , while the liquid phase is calculated based on  $\sum_{k=1}^n \alpha_k = 1$ . Therefore,  $\alpha_1 = 1 - \alpha_i$ , where  $\alpha_i = \sum_{k=2}^n \alpha_k$ . In Eqs. (A.2) and (A.4), 3 parameters  $\mathbf{u}_{km}$ ,  $v_m$  and  $v_m^t$  require a closure relation. Starting with  $\mathbf{u}_{km}$ , using the relative velocity approach, we use the following equation that is based on the work of Lockett and Bassoon (1979), Masliyah (1979):

$$\mathbf{u}_{km} = \mathbf{u}_{kr} - \sum_{k=1}^n c_k \mathbf{u}_{kr}, \quad (\text{A.5})$$

where  $\mathbf{u}_{kr} = \mathbf{u}_k - \mathbf{u}_l$  is the relative velocity of the solid phase  $u_k$  to liquid phase  $u_l$ , also known as the terminal settling velocity. The constitutive equation of the terminal settling velocity is described more in detail in Appendix C.

The presence of sediment particles in the liquid will affect the kinematic viscosity of the mixture  $v_m$ . Thus, we use a formula to account for the change in the mixture viscosity (Thomas, 1965), noting that the mixture still falls into the Newtonian regime. The mixture viscosity equation can be described as follows:

$$v_m = v_f(1 + 2.5\alpha_i + 10.05\alpha_i^2 + A \exp(B\alpha_i)), \quad (\text{A.6})$$

where  $A$  and  $B$  are empirical factors that are taken to be  $= 0.00273$  and  $16.6$ , respectively (Goeree, 2018).

In this study, the buoyant  $k-\epsilon$  model is used to capture the influence of turbulence. This model is a modification version of the standard  $k-\epsilon$  model. Such that the employed model takes the density gradient into consideration.

The Buoyant  $k-\epsilon$  model can be described by the following equations (Henkes et al., 1991):

$$\frac{\partial \rho_m k}{\partial t} + \nabla \cdot (\rho_m k \mathbf{u}_m) = \nabla \cdot \left[ \left( v_m + \frac{v_m^t}{\sigma_k} \right) \nabla k \right] + P_k + P_b + \rho_m \epsilon, \quad (\text{A.7})$$

$$\frac{\partial \rho_m \epsilon}{\partial t} + \nabla \cdot (\rho_m \epsilon \mathbf{u}_m) = \nabla \cdot \left[ \left( v_m + \frac{v_m^t}{\sigma_\epsilon} \right) \nabla \epsilon \right] + C_{11} \frac{\epsilon}{k} (P_k + C_{13} P_b) - C_{12} \rho_m \frac{\epsilon^2}{k}, \quad (\text{A.8})$$

where  $k$  is turbulent kinetic energy,  $\sigma_k = 1$  and  $\sigma_\epsilon = 1.3$  are the turbulent Prandtl numbers,  $C_{11} = 1.44$ ,  $C_{12} = 1.92$ , and  $C_{13} = 1$  are turbulence model constants,  $P_b$  is the generation of turbulent kinetic energy due to buoyancy, and  $P_k$  is the generation of turbulent kinetic energy due to mean velocity gradients. After solving the  $k-\epsilon$  model, eddy viscosity  $v_m^t$  can be calculated:

$$v_m^t = C_\mu \frac{k^2}{\epsilon}, \quad (\text{A.9})$$

where  $C_\mu = 0.09$  is a turbulence constant.

## Appendix B. Population balance equation (PBE)

Aggregation and breakup are the two main processes that govern phase transition among solid particles. Despite flocculation being a complex process, Hounslow et al. (1988) presents a simple discretized equation that captures the transition of particles between phases. This discretization approach is based on size classes or size groups, in which the entire size range of sediment particles is divided into a specific number of groups. Each individual class is identified by its size, meaning that class  $k$  contains one size-based fraction. For simplicity, each class is treated as a phase, with the subscript  $k$  representing the class. The discretization approach is based on the idea that the volume of a particle in phase  $k+1$  is double that of a particle in phase  $k$ .

$$v_{k+1} = 2v_k, \quad (\text{B.1})$$

where  $v_k$  is the particle size in class  $k$ . Bearing this in mind, the discretized form of PBE can be described as follows:

$$\begin{aligned} \frac{dN_k}{dt} = & \sum_{j=1}^{k-2} 2^{j-k+1} \gamma \beta_{k-1,j} N_{k-1} N_j + \frac{1}{2} \gamma \beta_{k-1,k-1} N_{k-1}^2 \\ & - N_k \sum_{j=1}^{k-1} 2^{j-k} \gamma \beta_{k,j} N_j - N_k \sum_{j=k}^{kmax} \gamma \beta_{k,j} N_j \\ & - S_k N_k + \sum_{j=i}^{imax} \zeta_{k,j} S_j N_j, \end{aligned} \quad (\text{B.2})$$

where  $N_k$  ( $\#/m^3$ ) =  $\alpha_k/v_k$  is the number concentration in particles of phase  $k$ ,  $\gamma$  is the collision efficiency,  $\beta_{k,j}$  ( $m^3/s$ ) is the collision frequency between particles in groups  $k$  and  $j$ ,  $S_k$  ( $s^{-1}$ ) is the breakage rate of particles in group  $k$  and  $\zeta$  is the breakage distribution function which determines the volume fraction of particles of group  $k$  resulting from the fragmentation of particles of group  $j$ . Fig. B.1 provides a graphical representation of the RHS source terms of Eq. (B.2),

in which four functions that represent the particulate system are present; these functions are:

1. Collision efficiency  $\gamma$ ,
2. Collision frequency  $\beta_{k,j}$ ,
3. Breakage rate  $S_k$ ,
4. Breakage distribution function  $\zeta$ .

Such functions require closures, as they are the main driver of the phase transition process. Each closure will be discussed in the following subsections.

### B.1. Collision efficiency ( $\gamma$ )

The aggregation probability between two particles from different phases  $k$  and  $j$  can be described by the collision efficiency  $\gamma$ , which ranges from 0 to 1. When every collision results in floc formation,  $\gamma = 1$ . On the other hand, when no collision leads to floc formation,  $\gamma = 0$ . Determining the collision efficiency is a complex process as it depends on the surface properties of the particles, interaction forces between particles, and hydrodynamic effects within the aggregate. In some cases,  $\gamma$  is considered as a constant value (Biggs and Lant, 2002; Golzarjalal et al., 2018), while in others, it is considered as an adjustable parameter (Zhang and Li, 2003; Wickramasinghe et al., 2005). In this study, the value of  $\gamma$  is assumed to be 0.5 for all simulations.

### B.2. Collision frequency ( $\beta_{k,j}$ )

Assessing the frequency of collisions is challenging due to the intricate interaction of various factors, including: (i) Perikinetic aggregation of flocs, i.e. Brownian motion,  $\beta_{k,j}^{Br}$ , (ii) Orthokinetic aggregation of flocs, i.e. aggregation occurs because of a velocity gradient in a fluid,  $\beta_{k,j}^{sh}$ , (iii) Gravity aggregation, i.e. differential settling,  $\beta_{k,j}^g$ . For any given two particles, each of which belongs to a different phase  $k$  or  $j$ , collision frequency is calculated as follows:

$$\beta_{k,j} = \beta_{k,j}^{Br} + \beta_{k,j}^{sh} + \beta_{k,j}^g. \quad (\text{B.3})$$

The flocs resulting from an aggregation process are irregular, permeable structures. Two parameters are introduced by Veerapaneni and Wiesner (1996) to correct for the fluid collision efficiency, (i) The efficiency of fluid accumulation inside a floc  $\eta$ , (ii) The ratio of the drag force of a permeable aggregate to the drag force of an impermeable aggregate  $\Omega$ . The collision efficiency between permeable and irregular flocs is thus given by the following equations:

$$\beta_{k,j}^{Br} = \frac{2k_b T}{3\mu} \left( \frac{1}{\Omega_k r_k} + \frac{1}{\Omega_j r_j} \right) (r_k + r_j), \quad (\text{B.4})$$

$$\beta_{k,j}^{sh} = 1.294G \left( \sqrt{\eta_k} r_k + \sqrt{\eta_j} r_j \right)^3, \quad (\text{B.5})$$

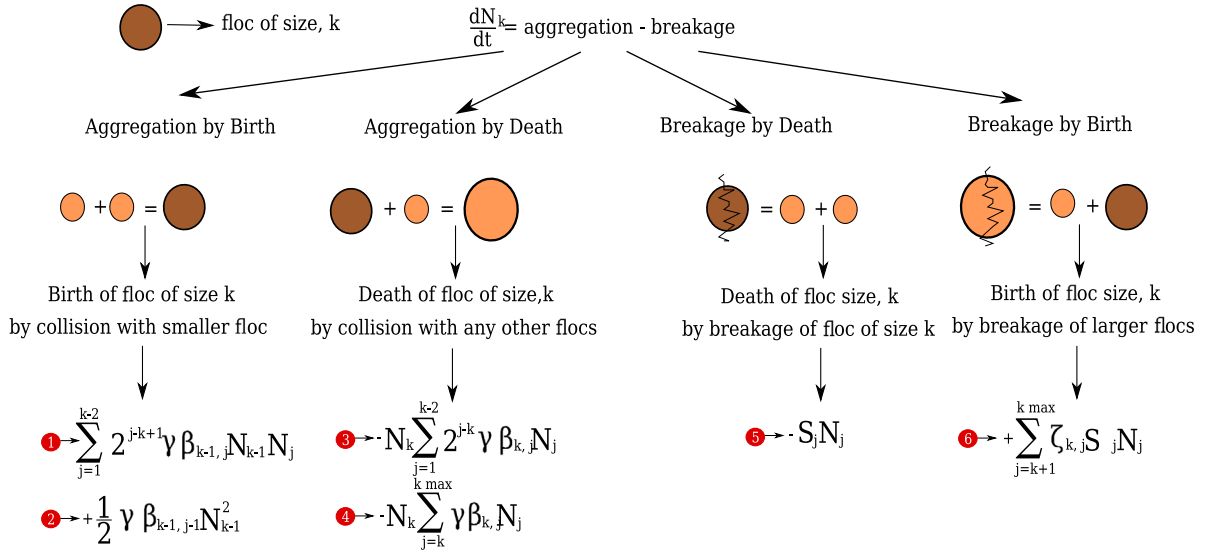


**Fig. B.1.** Aggregation and breakage dynamics of the discretized PBE, Eq. (B.2), adapted from Biggs and Lant (2002). Following Eq. (B.2), first term is formation of floc  $k$  due to collision of unequal particle sizes, second term is formation of floc  $k$  due to collision of equal particle sizes, third term is death of floc  $k$  due to collision with smaller particles, fourth term is death of floc  $k$  due to collision with equal or large particles, fifth term is death of floc  $k$  due to breakage, sixth term is formation of floc  $k$  due to breakage of large particles.

$$\beta_{k,j}^g = \pi \left( \sqrt{\eta_k} r_k + \sqrt{\eta_j} r_j \right)^2 |u_{kr} - u_{jr}|, \quad (\text{B.6})$$

where  $r_k$  is the effective capture radius of an aggregate of phase  $k$ ,  $k_b$  is Boltzmann constant,  $T$  is the temperature,  $G = (c/\nu)^{1/2}$  is the shear rate and  $\mu$  is the dynamic viscosity. Considering the fractal dimension, the value of a floc's effective radius is determined by the following equation (Flesch et al., 1999):

$$r_k = r_2 \left( \frac{v_k}{v_2} \right)^{1/d_f}, \quad (\text{B.7})$$

where  $r_2 = d_2/2$  is the primary particle radius,  $d_f$  is the fractal dimension, which ranges from 1 to 3, with 1 being line of particles and 3 is a solid sphere. The irregular shape and the permeability of a floc are governed by the value of  $d_f$ , making it a critical factor for flocs structure.  $\Omega$  in Eq. (B.4) is the ratio between the force exerted by the fluid on a permeable aggregate and the force exerted by the fluid on an impervious sphere of an equivalent size (Jeldres et al., 2015), it is given by:

$$\Omega = \frac{2\xi^2 \left( 1 - \frac{\tanh\xi}{\xi} \right)}{2\xi^2 + 3 \left( 1 - \frac{\tanh\xi}{\xi} \right)}, \quad (\text{B.8})$$

where  $\xi = r/\sqrt{K}$  is the dimensionless permeability, in which  $K$  is the permeability of an aggregate. We employ the Brinkman and Happel permeability equation to calculate the  $K$  (Li and Logan, 2001),

$$K = \frac{d_2^2}{72} \left( 3 + \frac{3}{1-\phi} - \sqrt[3]{\frac{8}{1-\phi} - 3} \right), \quad (\text{B.9})$$

where  $\phi$  is the porosity of a floc, which is calculated using the fractal dimension approach:

$$\phi = 1 - C_b \left( \frac{d_k}{d_2} \right)^{d_f-3}, \quad (\text{B.10})$$

where  $C_b$  is the packing coefficient, which is assumed to be 1 in this work. As demonstrated by Eq. (B.10), there is an inverse relationship between fractal dimension and floc porosity. As the fractal dimension increases, the floc porosity decreases. This trend continues until the fractal dimension reaches its maximum value of  $d_f = 3$ , at which point the floc porosity reaches its minimum value of 0, indicating a solid case with no voids or pores, (Li and Logan, 2001).

Following Eqs. (B.5) and (B.6) and the Brinkman equations (Wickramasinghe et al., 2005),  $\eta$  is calculated using the following equation (Biggs and Lant, 2002):

$$\eta = 1 - \frac{d}{\xi} - \frac{c}{\xi^3}, \quad (\text{B.11})$$

where

$$d = \frac{3}{J} \xi^3 \left( 1 - \frac{\tanh\xi}{\xi} \right), \quad (\text{B.12})$$

$$c = -\frac{1}{J} \left( \xi^5 + 6\xi^3 - \frac{\tanh\xi}{\xi} (3\xi^5 + 6\xi^3) \right), \quad (\text{B.13})$$

$$J = 2\xi^2 + 3 - 3 \frac{\tanh\xi}{\xi}. \quad (\text{B.14})$$

### B.3. Breakage rate ( $S_k$ )

In general, a floc breaks up when the imposed external force on the floc exceeds the floc's strength. The breakage rate  $S_k$  is determined as follows (Winterwerp, 1998):

$$S_i = E_b G \left( \frac{d_k - d_2}{d_2} \right)^{3-d_f} \left( \frac{\mu G}{F_y/d_k^2} \right)^{\frac{1}{2}} \quad (\text{B.15})$$

where  $F_y$  is floc strength. Very little is known about  $F_y$ , but (Van Leussen, 1994) estimated it to be approximately  $10^{-10}N$ .  $E_b$  is the breakage coefficient.

### B.4. Breakage distribution function

Determining the size distribution of daughter flocs produced from the breakup of a parent floc is challenging. Theoretical breakup distribution functions are used to find the best fit for the experimental data. In this study, we adopt a binary breakage function, which we believe will be adequate, as discussed in (Chen et al., 1990; Jeldres et al., 2015).

$$\zeta_{k,j} = \frac{v_j}{v_k}, \quad j = k+1 \text{ and } \zeta_{k,j} = 0 \text{ for } j \neq k+1 \quad (\text{B.16})$$

B.5. Coupling between drift-flux model and PBE

We couple fluid dynamics and phase transition by using the relationship between the number density  $N_k$  and the volume concentration of particle phase, which remains constant over time.

$$N_k = \frac{\alpha_k}{v_k}. \tag{B.17}$$

From Eq. (B.17) and Eq. (A.4) we can deduce the following equation:

$$\begin{aligned} \frac{\partial \alpha_k}{\partial t} + \nabla \cdot (\alpha_k (\mathbf{u}_m + \mathbf{u}_{km})) = & \left[ v_k \sum_{j=1}^{k-2} 2^{j-k+1} \gamma \beta_{k-1,j} N_{k-1} N_j \right. \\ & + \frac{1}{2} v_k \gamma \beta_{k-1,k-1} N_{k-1}^2 - v_k N_k \sum_{j=1}^{k-1} 2^{j-k} \gamma \beta_{k,j} N_j - \\ & \left. v_k N_k \sum_{j=1}^{imax} \gamma \beta_{k,j} N_j - S_k N_k v_k + v_k \sum_{j=1}^{imax} \zeta_{k,j} S_j N_j \right] + \nabla \cdot \Gamma_t \nabla \alpha_k \end{aligned} \tag{B.18}$$

Thus, we replace Eq. (A.4) by Eq. (B.18), obtaining a particle of phase  $k$  that travels through time, space (advection and diffusion), and phase domains (i.e, volume as an internal coordinate)

Appendix C. Settling velocity

Investigating flocculation issues requires a close examination of the PSD, as it plays a crucial role in determining the effects of flocculation on mixture hydrodynamics. The PSD of CCZ is analysed by Gillard et al. (2019), and the results provide a key starting point for further modelling efforts (as seen in Fig. C.1).

The PSD used in this study is taken from the 8MUC location and divided into 27 fractions. The smallest fraction, known as the ‘‘primary phase’’, is  $d_{k=2} = 2 \mu\text{m}$  with density  $\rho_{k=2} = 2650$ . The largest fraction, which is based on the maximum floc size found by Gillard et al. (2019) in three experimental cases, is  $d_{k=28} = 812.74 \mu\text{m}$  (refer to Fig. C.1). The intermediate fractions were calculated using the discretization rule in Eq. (B.1). Note that a correction is made to the 27 fraction PSD curve to ensure that the area under the curve remains equal to one. This correction is necessary to account for the difference between the original PSD curve of Gillard et al. (2019) and the selected PSD used in this study.

In shear-induced flows, aggregation of particles results in an increase in floc size and a decrease in density as water becomes trapped within the flocs during the aggregation process. This has a direct impact on the settling velocity of the flocs, which then affects the accuracy of predictions for mixture hydrodynamics. To account for these changes, we use an improved definition of settling velocity that takes into account the floc density by incorporating the primary particle size ( $d_{k=2}$ ) and the fractal dimension ( $d_f$ ). This updated formula extends the one proposed by Ferguson and Church (2004) and is as follows:

$$u_{kr} = \frac{R_{s,k} g d_k^2}{b_1 v_c + (0.75 b_2 R g d_k^3)^{1/2}}, \tag{C.1}$$

where  $v_c$  is the kinematic viscosity of the carrier fluid (water), and  $b_1$  and  $b_2$  are coefficients that account for particle shape and drag, respectively.  $R_{s,k} = (\rho_k - \rho_1) / \rho_k$  represents the submerged specific gravity and highlights the correlation between floc density and settling velocity.  $R_{s,k}$  is calculated differently as per Kranenburg (1994), Strom and Keyvani (2011), as follows:

$$R_{f,k} = R_{s,k} \left( \frac{d_k}{d_2} \right)^{d_f - 3}, \tag{C.2}$$

By substituting Eq. (C.2) with Eq. (C.1), we arrive at a general explicit formulation for the settling velocity of a floc as follow:

$$u_{kr} = \frac{R g d_k^{d_f - 1}}{b_1 v_c d_2^{d_f - 3} + b_2 (0.75 R g d_k^{d_f} d_2^{d_f - 3})^{1/2}}, \tag{C.3}$$

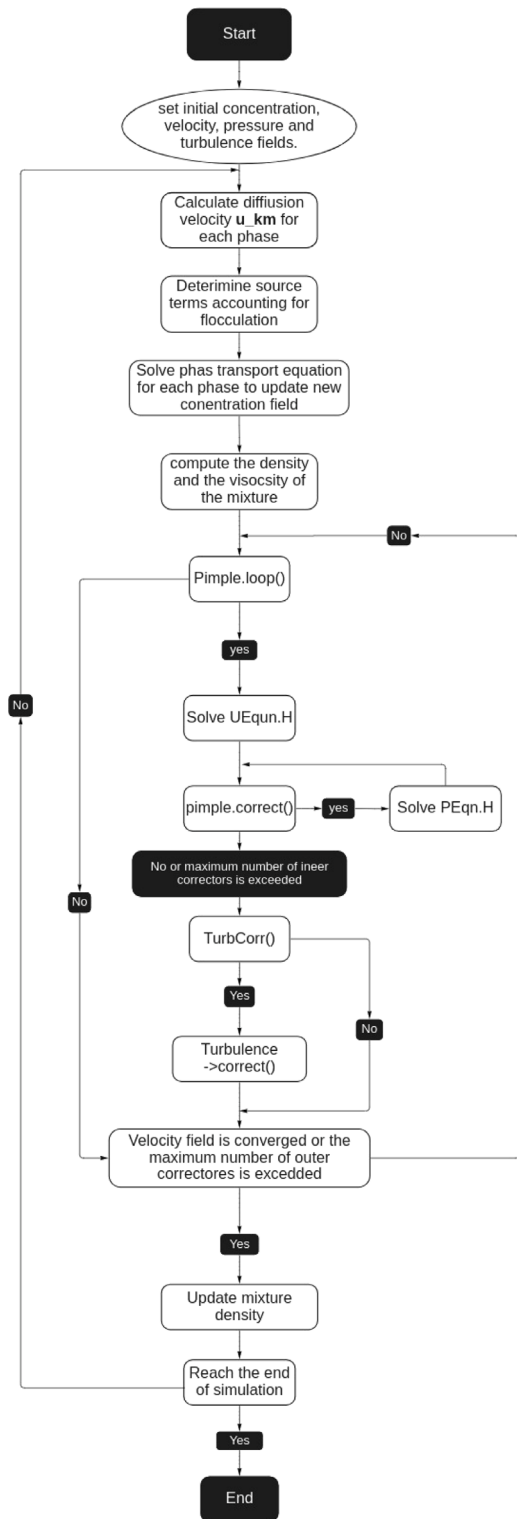


Fig. B.2. Flow chart of the solver algorithm in OpenFOAM.

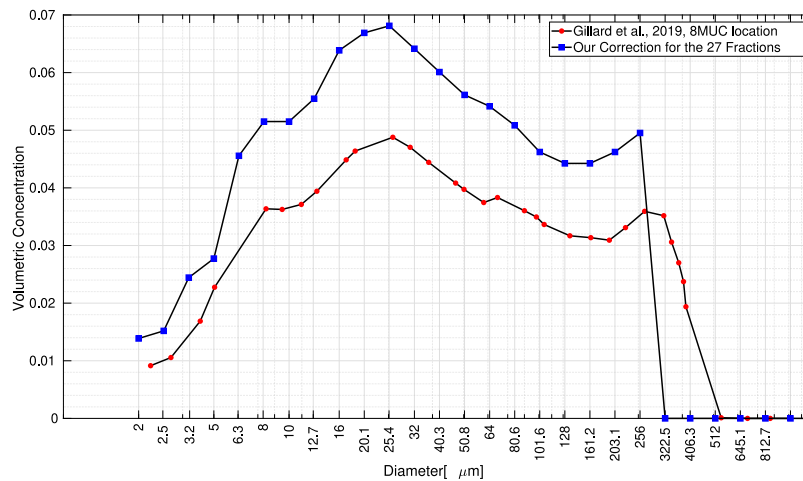


Fig. C.1. PSD of the 8 MUC location in the CCZ (Gillard et al., 2019). The blue points represents the corrected 27 fractions used in this work.

## References

- Alhaddad, S., Helmons, R., 2023. Sediment Erosion generated by a Coandă-effect-based polymetallic-nodule collector. *J. Mar. Sci. Eng.* 11 (2), 349.
- Alhaddad, S., Mehta, D., Helmons, R., 2022. Mining of deep-seabed nodules using a coandă-effect-based collector. *Results Eng.* 100852.
- Alhaddad, S., de Wit, L., Labeur, R.J., Uijtewaal, W., 2020. Modeling of breaching-generated turbidity currents using large eddy simulation. *J. Mar. Sci. Eng.* 8 (9), 728.
- Ali, W., Enthoven, D., Kirichek, A., Chassagne, C., Helmons, R., 2022. Effect of flocculation on turbidity currents. *Front. Earth Sci.* 10, 1014170.
- Bhole, M., Joshi, J., Ramkrishna, D., 2008. CFD simulation of bubble columns incorporating population balance modeling. *Chem. Eng. Sci.* 63 (8), 2267–2282.
- Biggs, C., Lant, P., 2002. Modelling activated sludge flocculation using population balances. *Powder Technol.* 124 (3), 201–211.
- Cahill, J., Cummins, P., Staples, E., Thompson, L., 1987. Size distribution of aggregates in flocculating dispersions. *J. Colloid Interface Sci.* 117 (2), 406–414.
- Chen, W., Fischer, R.R., Berg, J.C., 1990. Simulation of particle size distribution in an aggregation-breakup process. *Chem. Eng. Sci.* 45 (9), 3003–3006. [http://dx.doi.org/10.1016/0009-2509\(90\)80201-O](http://dx.doi.org/10.1016/0009-2509(90)80201-O), URL <https://www.sciencedirect.com/science/article/pii/0009250990802010>.
- Chen, F., Simon, C., Lai, A.C., 2006. Modeling particle distribution and deposition in indoor environments with a new drift–flux model. *Atmos. Environ.* 40 (2), 357–367.
- de Wit, L., Talmon, A., Van Rhee, C., 2014. 3D CFD simulations of trailing suction hopper dredger plume mixing: Comparison with field measurements. *Mar. Pollut. Bull.* 88 (1–2), 34–46.
- Decrop, B., Wachter, T.D., 2019. Detailed CFD Simulations For near Field Dispersion Of Deep Sea Mining Plumes. pp. 116–127.
- Delft High Performance Computing Centre (DHPC), 2022. DelftBlue supercomputer (phase 1). <https://www.tudelft.nl/dhpc/ark:/44463/DelftBluePhase1>.
- Elerian, M., Alhaddad, S., Helmons, R., van Rhee, C., 2021. Near-field analysis of turbidity flows generated by polymetallic nodule mining tools. *Mining* 1 (3), 251–278.
- Elerian, M., Van Rhee, C., Helmons, R., 2022. Experimental and numerical modelling of deep-sea-mining-generated turbidity currents. *Minerals* 12 (5), <http://dx.doi.org/10.3390/min12050558>, URL <https://www.mdpi.com/2075-163X/12/5/558>.
- Ferguson, R., Church, M., 2004. A simple universal equation for grain settling velocity. *J. Sediment. Res.* 74 (6), 933–937.
- Fernández-Barbero, A., Schmitt, A., Cabrerizo-Vílchez, M., Martínez-García, R., 1996. Cluster-size distribution in colloidal aggregation monitored by single-cluster light scattering. *Physica A* 230 (1–2), 53–74.
- Flesch, J.C., Spicer, P.T., Pratsinis, S.E., 1999. Laminar and turbulent shear-induced flocculation of fractal aggregates. *AIChE J.* 45 (5), 1114–1124.
- Gillard, B., Purkiani, K., Chatzievangelou, D., Vink, A., Iversen, M.H., Thomsen, L., Ackley, S.F., 2019. Physical and hydrodynamic properties of deep sea mining-generated, abyssal sediment plumes in the clarion clipperton fracture zone (eastern-central Pacific). *Elementa: Sci. Anthropocene* 7.
- Gillard, B., Thomsen, L., 2019. Characterization of sediment plumes behind mining vehicles in the NORI area (laboratory analyses). Tech. rep. iSeaMC.
- Goeree, J., 2018. Drift-flux modeling of hyper-concentrated solid-liquid flows in dredging applications (Ph.D. thesis). Delft University of Technology, <http://dx.doi.org/10.4233/uuid:2d432d11-ccc4-40de-b951-e89dfefebf27>.
- Golzarjalal, M., Zokaee Ashtiani, F., Dabir, B., 2018. Modeling of microalgal shear-induced flocculation and sedimentation using a coupled CFD-population balance approach. *Biotechnol. Prog.* 34 (1), 160–174.
- GSR, G.S.M.R., 2018. Environmental Impact Statement: Small-scale testing of nodule collector components on the seafloor of the Clarion-Clipperton Fracture Zone and its environmental impact. Tech. rep., Global Sea Mineral Resources NV.
- Harris, T.C., Hogg, A.J., Huppert, H.E., 2002. Polydisperse particle-driven gravity currents. *J. Fluid Mech.* 472, 333–371.
- Helmons, R., de Wit, L., de Stigter, H., Spearman, J., 2022. Dispersion of benthic plumes in deep-sea mining: What lessons can be learned from dredging? *Front. Earth Sci.* 796.
- Henkes, R., Van Der Vlugt, F., Hoogendoorn, C., 1991. Natural-convection flow in a square cavity calculated with low-Reynolds-number turbulence models. *Int. J. Heat Mass Transfer* 34 (2), 377–388.
- Hounslow, M., Ryall, R., Marshall, V., 1988. A discretized population balance for nucleation, growth, and aggregation. *AIChE J.* 34 (11), 1821–1832.
- Jankowski, J., Malcherek, A., Zielke, W., 1994. Numerical modeling of sediment transport processes caused by deep sea mining discharges. In: *Proceedings of OCEANS'94*, Vol. 3. IEEE, pp. III–269.
- Jeldres, R.I., Concha, F., Toledo, P.G., 2015. Population balance modelling of particle flocculation with attention to aggregate restructuring and permeability. *Adv. Colloid Interface Sci.* 224, 62–71.
- Kranenburg, C., 1994. The fractal structure of cohesive sediment aggregates. *Estuar. Coast. Shelf Sci.* 39 (5), 451–460.
- Li, X.-Y., Logan, B.E., 2001. Permeability of fractal aggregates. *Water Res.* 35 (14), 3373–3380.
- Lockett, M.J., Bassoon, K., 1979. Sedimentation of binary particle mixtures. *Powder Technol.* 24 (1), 1–7.
- Maggi, F., 2009. Biological flocculation of suspended particles in nutrient-rich aqueous ecosystems. *J. Hydrol.* 376 (1–2), 116–125.
- Masliyah, J.H., 1979. Hindered settling in a multi-species particle system. *Chem. Eng. Sci.* 34 (9), 1166–1168.
- Mietta, F., Chassagne, C., Verney, R., Winterwerp, J.C., 2011. On the behavior of mud flow size distribution: Model calibration and model behavior. *Ocean Dyn.* 61, 257–271.
- Muñoz-Royo, C., Ouillon, R., El Mousadik, S., Alford, M.H., Peacock, T., 2022. An in situ study of abyssal turbidity-current sediment plumes generated by a deep seabed polymetallic nodule mining preprototype collector vehicle. *Sci. Adv.* 8 (38), eabn1219.
- Ouillon, R., Kakoutas, C., Meiburg, E., Peacock, T., 2021. Gravity currents from moving sources. *J. Fluid Mech.* 924.
- Purkiani, K., Gillard, B., Paul, A., Haecel, M., Haalboom, S., Greinert, J., Stigter, H.D., Hollstein, M., Baeye, M., Vink, A., et al., 2021. Numerical simulation of deep-sea sediment transport induced by a dredge experiment in the northeastern Pacific ocean. *Front. Mar. Sci.* 1175.
- Quezada, G.R., Ayala, L., Leiva, W.H., Toro, N., Toledo, P.G., Robles, P., I Jeldres, R., 2020. Describing mining tailing flocculation in seawater by population balance models: Effect of mixing intensity. *Metals* 10 (2), 240.
- Ruan, Z., Wu, A., Bürger, R., Betancourt, F., Ordoñez, R., Wang, J., Wang, S., Wang, Y., 2021. A population balance model for shear-induced polymer-bridging flocculation of total tailings. *Minerals* 12 (1), 40.
- Russel, W.B., Russel, W., Saville, D.A., Schowalter, W.R., 1989. *Colloidal dispersions*. Cambridge University Press.
- Sharma, R., 2015. Environmental issues of deep-sea mining. *Procedia Earth Planet. Sci.* 11, 204–211.
- Shen, X., Lee, B.J., Fettweis, M., Toorman, E.A., 2018. A tri-modal flocculation model coupled with TELEMAC for estuarine muds both in the laboratory and in the field. *Water Res.* 145, 473–486.

- Shi, Z., Zhang, G., Zhang, Y., He, T., Pei, G., 2019. Modeling of flocculation and sedimentation using population balance equation. *J. Chem.* 2019.
- Silva, L.F.L., Damian, R., Lage, P.L., 2008. Implementation and analysis of numerical solution of the population balance equation in CFD packages. *Comput. Chem. Eng.* 32 (12), 2933–2945.
- Spearman, J., Taylor, J., Crossouard, N., Cooper, A., Turnbull, M., Manning, A., Lee, M., Murton, B., 2020. Measurement and modelling of deep sea sediment plumes and implications for deep sea mining. *Sci. Rep.* 10 (1), 1–14.
- Strom, K., Keyvani, A., 2011. An explicit full-range settling velocity equation for mud flocs. *J. Sediment. Res.* 81 (12), 921–934.
- Thomas, D.G., 1965. Transport characteristics of suspension: VIII. A note on the viscosity of Newtonian suspensions of uniform spherical particles. *J. Colloid Sci.* 20 (3), 267–277.
- Van Leussen, W., 1994. Estuarine macroflocs and their role in fine-grained sediment transport. ministry of transport. Public Works and Water Management, National Institute for Coastal and Marine Management (RIKZ).
- Van Rhee, C., 2002. On the sedimentation process in a trailing suction hopper dredger (Ph.D. thesis). Delft University of Technology.
- Veerapaneni, S., Wiesner, M.R., 1996. Hydrodynamics of fractal aggregates with radially varying permeability. *J. Colloid Interface Sci.* 177 (1), 45–57.
- Wickramasinghe, S., Han, B., Akeprathumchai, S., Jaganjac, A., Qian, X., 2005. Modeling flocculation of biological cells. *Powder Technol.* 156 (2–3), 146–153.
- Winterwerp, J.C., 1998. A simple model for turbulence induced flocculation of cohesive sediment. *J. Hydraul. Res.* 36 (3), 309–326.
- Zhang, J.-j., Li, X.-y., 2003. Modeling particle-size distribution dynamics in a flocculation system. *AIChE J.* 49 (7), 1870–1882.
- Zielke, W., Jankowski, J., Sündermann, J., Segschneider, J., 1995. Numerical modeling of sediment transport caused by deep-sea mining. In: First ISOPE Ocean Mining Symposium. OnePetro.